Late Quaternary slip rates across the central Tien Shan, Kyrgyz Republic, Central Asia

Stephen C. Thompson, University of Washington, Department of Earth and Space Sciences, Seattle, Washington
Ray J. Weldon, University of Oregon, Department of Geological Sciences, Eugene, Oregon
Charles M. Rubin, Central Washington University, Department of Geological Sciences, Ellensburg, Washington
Peter Molnar, Massachusetts Institute of Technology, Department of Earth, Atmosphere, and Planetary Sciences, Cambridge, Massachusetts[1]
Kanatbek Abdrakhmatov, Academy of Science, Kyrgyz Institute of Seismology, Bishkek, Kyrgyz Republic
Glenn W. Berger, Desert Research Institute, Reno, Nevada

[1]Now at: University of Colorado at Boulder, Department of Geological Sciences and CIRES, Boulder, Colorado

---

Abstract

Late Quaternary slip rates across active faults and folds show that active faulting is distributed across the Kyrgyz central Tien Shan, and not concentrated at its margins. Slip rates on eight faults in five basins, distributed over almost two thirds of the width of the central Tien Shan, range from ~0.1 to ~3 mm/yr. Virtually every intermontane basin contains Neogene and Quaternary syntectonic strata deformed by Holocene north-south shortening on thrust or reverse faults. Fault slip rates come from measurements of faulted and folded river terrace profiles and trench wall exposures. Radiocarbon, optically stimulated luminescence, and thermoluminescence ages constrain ages of numerous terraces and justify correlation in other basins. Monte Carlo simulations that sample from normally distributed and discrete probability distributions for each variable in the slip-rate calculations generate most likely slip-rate values and 95% confidence limits. Faults in basins appear to merge at relatively shallow depths with crustal-scale ramps that underlie mountain ranges composed of pre-

Cenozoic rocks. The similarity between current rates of north-south shortening measured using Global Positioning System (GPS) geodesy since 1993 and the sum of late Quaternary rates of shortening suggests that deformation is concentrated along major fault zones near range-basin margins, and slip on such faults separating essentially rigid blocks may best represent finite deformation in the upper crust.

1. Introduction

Different ideas, if not theories, of mountain building anticipate different spatial and temporal partitioning of strain during the growth of mountain belts. In many convergent belts, particularly in plate boundary settings, a polarity is manifested by a dominant vergence as well as by a unidirectional propagation of major faults that incorporate material by frontal accretion [e.g., *Bally et al.*, 1986; *Butler*, 1986; *Dahlstrom*, 1970; *Le Fort*, 1975; *Mattauer*, 1975; *Royse et al.*, 1975]. These characteristics are generally associated with simple shear on a gently dipping fault that underlies the belt [e.g., *Cook et al.*, 1979; *Mugnier et al.*, 1990; *Nelson and others*, 1996], a boundary condition that invites the application of critical wedge theory to examine convergent mountain building [*Dahlen*, 1984; *Davis et al.*, 1983; *Willett*, 1992]. Originally the shortening rates across these thrust belts was believed to be localized at the frontal fault [e.g., *Boyer and Elliott*, 1982; *Dahlstrom*, 1970], and field studies show that this condition does exist in nature, at least at one prominent belt [*Lavé and Avouac*, 2000]. Geologic [e.g., *Boyer*, 1992], analog [e.g., *Koyi et al.*, 2000], and numerical [*Willett*, 1999] studies, however, show that strain rates can not only be concentrated at a frontal fault, but also distributed across the entire deforming orogen.

Other convergent mountain belts, often classified as "thick-skinned" and which lie away from plate boundaries, lack a dominant direction of vergence, tend to consist of more widely spaced, fault bounded ranges and basins, and are not clearly associated with an underlying low-angle fault [e.g., *Gries*, 1983; *Jordan and Allmendinger*, 1986; *Molnar and Tapponnier*, 1975; *Rodgers*, 1987; *Tapponnier and Molnar*, 1979]. Although Earth scientists have long recognized differences among convergent mountain belts, inferences about the partitioning of strain rate across "thick-skinned" belts have been based on geological and geophysical observations with mostly qualitative results. In this paper, we examine how strain rate is partitioned across a "thick-skinned" convergent mountain belt within a continental interior. Theories of mountain-belt growth must predict and explain these geometric and kinematic constraints.

The Tien Shan of central Asia is a distant manifestation of continuing India-Eurasia plate convergence and exemplifies late Cenozoic mountain building by distributed deformation [e.g., *Burbank et al.*, 1999; *Cobbold et al.*, 1994; *Makarov*, 1977; *Sadybakasov*, 1972; 1990; *Schulz*, 1948; *Tapponnier and Molnar*, 1979]. Most investigations of active tectonics in the Tien Shan thus far have focused on the timing and rates of slip on thrust fault systems that bound the northern and southern margins [*Avouac et al.*, 1993; *Brown et al.*, 1998; *Burchfiel et al.*, 1999; *Yin et al.*, 1998]. Thus, the relative partitioning of late Quaternary geologic shortening among faults in the interior and at the margins of the belt has not been quantified. We present measurements of late Quaternary rates of slip on faults across the width of the Kyrgyz central Tien Shan, using river terraces and alluvial fans present within late Cenozoic basins as strain markers to measure displacements caused by shallow faulting and folding. Our motivation is to address questions related to how strain rates are distributed. For example, do faults on the margins of the mountain belt accommodate a higher proportion of strain rate than faults within the interior of the belt? Does slip on major faults account for all or most of the total strain-rate field, or is a significant portion of upper crustal strain accommodated by penetrative deformation away from major faults?

2. Tectonic and geologic setting

The elongate central and eastern Tien Shan represents a deforming region between two generally stable crustal elements: the Kazakh platform to the north and the Tarim basin to the south (Figure 1). Located ~1000-1500 km north of the Indo-Eurasian plate boundary, Global Positioning System (GPS) measurements suggest current shortening across the central Tien Shan presently absorbs nearly one-half of the total relative plate convergence [*Abdrakhmatov et al.*, 1996; *DeMets et al.*, 1994; *Holt et al.*, 2000].

The central Tien Shan display a range-basin topography that reflects late Cenozoic relief caused by distributed reverse faulting and folding [*Chediya*, 1986; *Makarov*, 1977; *Sadybakasov*, 1972; 1990; *Schulz*, 1948; *Tapponnier and Molnar*, 1979] (Figures 1 and 2). The generally east-west trending ranges of the central Tien Shan define folded and fault-bounded blocks that comprise previously deformed Paleozoic rocks [e.g., *Burtman*, 1975; *Knauf*, 1976] separated by basins of syntectonic Cenozoic sediment. A widespread, originally sub-planar, Mesozoic - early Cenozoic erosion surface serves as a strain marker for late Cenozoic deformation, and shows > 5 km of structural relief across several intermontane basin margins [*Makarov*, 1977; *Sadybakasov*, 1972; *Schulz*, 1948].

Historical seismicity and geodesy provide clues about the present-day deformation field across the central Tien Shan. The ~13 mm/yr GPS-measured north-south shortening rate across the northern 2/3 of the central Tien Shan is evenly distributed [*Abdrakhmatov et al.*, 1996; *Herring et al.*, manuscript in preparation]. Focal mechanisms from moderate and large earthquakes show primarily thrust and reverse faulting with P-axes oriented ~north-south, consistent with the geodetically measured maximum shortening direction and the overall direction of Indo-Eurasian plate convergence [e.g., *Ghose et al.*, 1998; *Nelson et al.*, 1987; *Ni*, 1978; *Shirokova*, 1974; *Tapponnier and Molnar*, 1979]. *Molnar and Ghose* [2000] find a rate of historical seismic-moment release across the central Tien Shan consistent with the rate of shortening measured by GPS, although uncertainties are large, and most moment release that they used occurred near the margins of deformation.

3. Distribution and character of late Quaternary faulting and folding

General similarities in active fault location, length, orientation, and sense of displacement exist from basin to basin (Figure 2). Holocene and late Pleistocene faults commonly lie within the basin interiors, a few to tens of kilometers from the range-basin margins, and slip at higher rates than faults that mark range-basin margins. The deformed hanging-wall strata and the narrow bands of differentially uplifted hills in the hanging walls of faults within the basins indicate fault-related folding and shallow flat-and-ramp-style deformation [*Suppe*, 1983]. The fault geometry indicates a transfer of displacement at depth from a steep crustal ramp that underlies the basin margin to a shallow fault that propagates into the basin sediment [*Ikeda*, 1983]. This kinematic relationship is common in the Tien Shan [e.g., *Avouac et al.*, 1993; *Brown et al.*, 1998; *Burchfiel et al.*, 1999; *Molnar et al.*, 1994] and other convergent orogens [e.g., *Benedetti et al.*, 2000; *Gries*, 1983; *Ikeda*, 1983; *Yeats and Lillie*, 1991]. Holocene and late Pleistocene fault traces can be discontinuous, with alternating buried and exposed fault tip lines, and many fault lengths are short relative to the basins and ranges they occupy or bound. Most faults strike east-west to east-northeast, following the general grain of previously deformed Paleozoic rocks visible in the ranges. Although several faults show evidence for dextral or sinistral components of motion, as revealed by exposed fault-plane striae or laterally deflected landforms [*Abdrakhmatov et al.*, in press; *Cobbold et al.*, 1994; *Makarov*, 1977], the majority of late Quaternary faults indicate dominantly dip-slip motion. The right-lateral strike-slip Talas-Ferghana fault [*Burtman*, 1964; *Burtman et al.*, 1996; *Trifonov et al.*, 1991], lying west of our study area, is a notable exception.

4. Fault slip rates – strategy and methods

Profiles of deformed river terraces, trench walls, natural exposures of faults, and radiocarbon and luminescence ages provide data for measuring fault slip rates. Appendices A and B illustrate the method for calculating slip rates for a simple case of an offset river terrace and the more complicated case of terraces deforming in response to fault-bend folding. Slip rates are presented with the most probable value and minimum and maximum 95% confidence values resulting from Monte Carlo simulations of uncertainties described in Appendix C. Unless specified otherwise, all uncertainties in the text represent the 2σ or 95% confidence interval. Below we explain the methods of collecting and analyzing data.

River terraces, representing ancient floodplains, occur along many river valleys that cross the margins of intermontane basins in the Kyrgyz Tien Shan [e.g., *Grigorienko*, 1970]. Because they represent potentially datable surfaces with known initial geometry, river terraces that cross active faults and folds make ideal strain markers for the study of rates and kinematics of deformation [e.g., *Avouac et al.*, 1993; *Lavé and Avouac*, 2000; *Molnar et al.*, 1994; *Rockwell et al.*, 1988; *Weldon and Sieh*, 1985].

We surveyed river terrace treads and fault scarps with a laser-distance theodolite (total station) and differential Global Positioning System receivers. Uncertainties in relative positions made with these instruments are less than a few decimeters and are less than the local variability in the position of the geologic contacts or geomorphic surfaces that we measured. The typical stratigraphy within a terrace includes a bedrock strath (most commonly formed on weakly cemented Tertiary sandstone and siltstone), one to several meters of coarse fluvial gravel, and a few centimeters to several meters of overlying fine-grained silt and sand, which we interpret to be a combination of overbank deposits, colluvium, and loess. For river terraces covered with thick or variable deposits of loess or colluvium, we surveyed the contact between fluvial gravel and overlying fine-grained deposits. This contact is preferable to the strath as a strain marker, because 1) the strath appears to have formed at different times along the terrace profile, particularly depending on the local vertical component of slip [*Molnar et al.*, 1994], and 2) the samples collected for dating constrain the timing of river incision and terrace formation that is represented in the stratigraphy by the gravel/fine-grained deposit contact. We assume that the terraces originally formed parts of planar surfaces over distances of several hundred meters to a few kilometers.

Geologic mapping at each site provides data to interpret the fault geometry and relate the terrace deformation to fault deformation. Because most late Quaternary faults we examined lie within the well bedded Cenozoic strata of intermontane basins, mapped bedding dips and fault traces enable preliminary cross-sections to be drawn that use simplified fault-related fold geometries [e.g., *Suppe*, 1983; *Suppe and Medwedeff*, 1990] and predict active and inactive axial surfaces and subsurface fault geometry in the absence of subsurface data. The terraces that cross these active faults have been deformed less than the Cenozoic strata; thus they are angular unconformities that can test the geometric and kinematic predictions of fault-related fold deformation [e.g., *Arrowsmith and Strecker*, 1999; *Lavé and Avouac*, 2000] (Appendix B), not unlike growth strata [*Suppe et al.*, 1992].

Radiocarbon, thermoluminescence (TL), and infrared-stimulated luminescence (IRSL) ages constrain the timing of past river incision, floodplain abandonment, and river terrace formation, and hence are used to date the strain markers that we use for slip-rate calculations. The age data we have collected thus far indicate that certain river terraces within and between intermontane basins that have been correlated based on morphology [e.g., *Chediya*, 1986] formed during similar time intervals. Furthermore, the data are consistent with the hypothesis that the hydrologic changes that caused the paleo-river incision and terrace formation coincided with major changes in global climate, although the correlation of paleoclimate in continental interiors with global climate proxies such as sea-level change is tenuous [*Gillespie and Molnar*, 1995].

Calibrated radiocarbon ages of charcoal samples collected from the broad, paired "QIII(2)" terrace and immediately inset "QIII(3)" terrace [*Abdrakhmatov*, unpublished data] in four drainage basis and three intermontane basins are similar (Figure 3 and Table 1), and indicate that widespread river incision and terrace formation occurred during the transition between the most recent global glacial-interglacial transition [*Fairbanks*, 1989; *Imbrie et al.*, 1984]. Appendix C explains how we treat radiocarbon ages in our slip-rate calculations.

Silt overlying river gravel was collected for TL and IRSL dating from four older terraces mapped as “QII(2)” [*Abdrakhmatov*, unpublished data] along three drainages in different intermontane basins (Figure 3, Table 2). For a TL or IRSL age to represent the actual age of deposition, the silt grains within a sample must be sufficiently “bleached” by sunlight so as to empty heat- and light-sensitive electron traps [e.g. *Aitken*, 1985; *Aitken*, 1998]. All of the samples collected for analysis consist of silt to sandy silt from deposits 2-30 m thick that overlie fluvial gravel, and are interpreted to be a combination of flood overbank deposits, loess, and minor colluvium.

The four TL and IRSL ages are statistically similar at the 95% confidence interval, and have a pooled mean age and standard deviation (1σ) of 140.7 ± 8.5 ka (Figure 3 and Appendix C). We use the pooled mean age and standard deviation to represent the age of the QII(2) terrace in our slip-rate calculations (Appendix C). The pooled age distribution is consistent with terrace formation during the penultimate global glacial-interglacial transition, ~128-140 ka [*Henderson and Slowey*, 2000; *Imbrie et al.*, 1984; *Shackleton*, 2000].

Because most of our radiocarbon samples, and all of our TL and IRSL samples are derived from fine-grained material that overlies river gravel of the terraces, most of our ages represent minimum ages of paleo-river incision. Nevertheless, because of the close agreement between ages of terraces in different drainage basins, we infer that 1) paleo-river incision occurred rapidly along the reaches that cross the active faults, 2) deposition of sediments (and datable material) overlying river gravel occurred rapidly after river incision, and 3) the ages reflect the timing of sediment deposition (e.g., minimal inherited age of charcoal; complete resetting of electron traps in silt), at least within the range of measurement uncertainties.

5. Fault slip rates

We have calculated the slip rate of the most active fault (or faults) in each of five basins (Figure 2). All of these fault zones show evidence for Holocene activity, and for multiple slip events since late Pleistocene time (<~140 x 10^3 yr B.P.).

5.1. Issyk-Ata fault, Chu basin

The Issyk-Ata fault defines the northern deformation front for the central Tien Shan between ~74º and ~75° E longitude (Figures 2 and 4a). It extends at least 120 km from the Aksu River east to its surface termination near the Shamsi River [*Abdrakhmatov*, 1988]. As a moderately dipping thrust to reverse fault at the surface, the Issyk-Ata fault places Neogene sandstone and siltstone over Quaternary gravel. The Issyk-Ata fault merges at its western terminus with the Chonkurchak fault, that marks the boundary between pre-Cenozoic basement at the Kyrgyz Range front and late Cenozoic deposits in the western Chu basin (Figure 4a). Farther east, between the Ala-Archa and Alamedin Rivers, the Chonkurchak fault steps north and its eastward continuation is called the Shamsi-Tunduk fault. Late Pleistocene terraces near the Alamedin River are folded along portions of the Shamsi-Tunduk fault, although the amplitude of folding indicates minor late Quaternary surface shortening compared to the folded and faulted terraces above the Issyk-Ata fault. We interpret the Issyk-Ata fault as a splay from the Shamsi-Tunduk / Chonkurchak fault beneath the southern margin of the Chu basin. We estimate a slip rate for the Issyk-Ata fault on its central portion, where it crosses the Alamedin River (Figure 4b).

Nested river terraces can be traced along the Alamedin River for about 12 km from within the Kyrgyz Range front to the Issyk-Ata fault, just south of Bishkek (Figure 4). Starting about 5 km south of the Issyk-Ata fault, between the Alamedin and Ala-Archa Rivers, river terraces cover a prominent row of hills consisting of south-dipping Neogene strata (Figures 4b and 5) [*Abdrakhmatov*, 1988; *Chediya*, 1986]. Terrace risers along the Alamedin River expose a nearly continuous section of Neogene sedimentary rock dipping nearly uniformly at ~34 ± 2° S beneath the uplifted terrace section (Figures 5a and 6). We did not find Neogene strata outcropping south of the elevated portion of the terrace. North of the Issyk-Ata fault, in the footwall, coalescing alluvial fans indicate that the Alamedin River is aggrading there.

A profile of the contact between a thin layer of fluvial gravel (deposited on the Tertiary bedrock strath) and overlying fine-grained sediments for the QII(2) terrace clearly shows a back-tilted section along the southern edge, particularly when rotated to remove the ~1.7º modern river gradient (Figure 6). The back-tilted segment, which we interpret as a growing backlimb of a fault-bend fold, rises to 103 ± 1 m for 1.7 km approximately parallel to the modern river profile. The top of the backlimb and the northern end, close to the fault, are higher. This variation in height could be due to steep faults or fault-related folding that we did not detect in our mapping of Neogene strata, or could indicate an older terrace ~125 m above modern river level, and an inset terrace ~103 m above modern river level. The silt deposit on top of the terrace gravel and bedrock strath is up to 30 m thick and obscures the variation in height of the gravel contact when the terrace is viewed from a distance (Figure 5a).

We analyze the QII(2) terrace deformation using simple fault-bend fold models of structural growth (Appendix B). To test the geometry and kinematics of a structural interpretation, we compare the terrace profile to predictions of the deformation of a flat unconformity (river terrace) due to slip on an inferred fault (Figure B1).

A lack of structural data south of the high section of the QII(2) terrace along the Alamedin River hinders a complete analysis of fold growth (a more complete analysis of fold growth is possible for the Akchop Hills fault in Kochkor basin, described below). Nevertheless, the amount of fault slip may be calculated from the difference in heights of the QII(2) terrace across the fold backlimb (h_1-h_2), from ψ, the angle between the slope of the terrace backlimb and the stream gradient, and from δ_1, the angle between the fault and the stream gradient, which is assumed to be equivalent to the angle between the bedding and the stream, α_1 (Appendix B, Figure B1).

We interpret the ~36 ± 2º difference between the dips of Tertiary strata under the elevated terrace and the present gradient of the river to reflect δ_1. To estimate δ_2 (the angle of the fault south of the backlimb) we searched equation B2 iteratively for values consistent with measurements of δ_1 and ψ. A line fit to three surveyed points that define the QII(2) terrace backlimb makes an angle of ψ = 9.5 ± 1.5º S with the surface, but one pair of these points yields 17º (Figure 6). Because most violations of the ideal fault-bend-fold geometry will reduce measured values of ψ [*Thompson et al.*, 1999], we use a range of backlimb angles of ψ = 8-17º S in the error analysis. The change in height of the terrace across the backlimb of the fold, (h_1-h_2) is given by the difference between the height of the flat middle section of the uplifted terrace, h_1 = 103 ± 1 m, and the height of a point surveyed south of the growing backlimb (with an assigned uncertainty twice the value of the measured one), h_2 = 24 ± 2 m.

An IRSL age of 170 ± 50 ka constrains the age of the QII(2) terrace along the Alamedin River (Figure 3 and Table 2). The IRSL age was measured on silt sampled from ~2.5 m above an exposed contact between river gravel and ~30 m of overlying fine-grained material (Figures 5 and 6). We interpret the fine-grained layer as mostly loess, although overbank sediment may be preserved or mixed with loess near the base of the sediment. To reduce uncertainty, we use the pooled age of 141 ± 17 ka for the QII(2) terrace in our calculation (Appendix C).

Solving equation B2 for δ_2 yields a value for fault dip south of the fold of 18 ± 6º S, and equation B1 yields 290 +230/-20 m of fault slip. The slip rate on the Issyk-Ata fault at the Alamedin River is 2.1 +1.7/-0.3 mm/yr (Figure 6).

Equation B3 predicts that the modern Alamedin River has risen 53 +128/-17 m since QII(2) formation, which corresponds to a minimum footwall aggradation rate of 0.5 +1.0/-0.1 mm/yr. This rate is consistent with the 0.6 ± 0.3 mm/yr aggradation rate of Plio-Pleistocene gravel measured near the Noruz River, about 15 km east of the Alamedin River (Figure 4) [*Bullen*, in review].

5.2. Akchop Hills and South Kochkor faults, Kochkor Basin

Active faults and folds deform the southern margin of the Kochkor basin, an east-west-trending intermontane basin south of the Kyrgyz Range (Figures 2 and 7a). The South Kochkor fault follows the southern margin of the basin, placing Paleozoic metamorphic and igneous rock of the Terskey Ala-Too over weakly cemented Neogene sedimentary rocks [*Fedorovich*, 1935; *Sadybakasov*, 1972; *Schulz*, 1948; *Tarasov*, 1970]. Although this fault and proximal splays cut late Quaternary river terraces and alluvial fans, most of the late Quaternary surface deformation occurs several kilometers to the north, within the basin, and is expressed by a band of hills of folded Miocene to Pliocene Djuanarik Formation sandstone and siltstone (Figure 7b). Erosion and deposition by the Djuanarik River, which flows northward across the southern margin of Kochkor basin, has produced multiple, nested river terraces that are progressively deformed across the growing Akchop Hills [*Fedorovich*, 1935] (Figure 8). We surveyed profiles along five river terraces and mapped the underlying strata on the west side of the Djuanarik River to evaluate the subsurface geometry and rates of slip on faults along the southern margin of Kochkor basin (Figures 7b and 9). The presence of an abrupt topographic front at the northern edge of the Akchop hills and the south-dipping strata underlying the hills indicate that the Akchop Hills are underlain by a southward dipping thrust fault, hereafter called the Akchop Hills fault, that connects south of the range front with the South Kochkor fault.

We calculate slip rates for both faults from measurements of a deformed late Quaternary terrace, starting with the faster slipping Akchop Hills fault.

5.2.1. Akchop Hills fault

Profiles of three river terraces along the west side of the Djuanarik River, rotated to remove the ~0.7º modern river gradient, show progressive vertical movement and development of back-tilted sections (Figure 9). Because the structure is well approximated by kink-style geometry, relatively angular bends (axial surfaces) (Figures 7b and 9), we can use fault-bend fold theory to infer the geometry and kinematics of fault slip at depth (Appendix B). Synclinal axial surfaces, in particular, are angular along the Djuanarik River, and two synclinal axial surfaces in the Neogene stratigraphy in the back limb of the fold (Figure 7b) also mark bends in river terraces QII(2) and QIII(1) (Figure 9a), indicating that the axial surfaces are presently active. We assume that faults are parallel to hanging-wall strata in the backlimb of the fold (i.e., no hanging-wall cut-off).

We interpret the southern synclinal bend to result from fault-bend folding above a thrust ramp that steepens from $\delta_2 = 9 \pm 2°$ S to $\delta_1 = 18 \pm 2°$ S (Figure 9c). We calculate the slip on the underlying fault using the difference in height of the QII(2) terrace across axial surface (i) (Figure 9). The predicted backlimb angle (Equation B2) matches the measured backlimb angle well, supporting the geometric interpretation (Figure 9c).

TL and IRSL analyses of massive silt from the base of a ~4 m thick deposit overlying the fluvial gravel of the QII(2) terrace yield an age of 128 ± 26 ka since last exposure to light and/or heat (Table 2 and Figures 3, 8 and 9). We use the pooled age of the four QII(2) terraces, 141 ± 17 ka, as the age of terrace formation in our slip rate calculation (Appendix C). The dip-slip rate, using parameters described above and inserted into Equation B1, is 2.9 +1.6/-0.7 mm/yr (Figure 9d).

5.2.2. South Kochkor fault

We calculate a slip rate for the South Kochkor fault using the offset QII(2) terrace at the range front (Figures 7b and 10a). A profile of the QII(2) terrace across the fault extends 2.5 km south of the range front and a similar distance north, and shows an abrupt bend (axial surface (iii) in Figure 7b) and a back-tilted section beginning ~600 m south of the fault (Figure 10a). Within ~100 m of the fault, the gravel contact of the QII(2) terrace folds into an anticline next to the fault scarp. In the footwall, the QII(2) terrace and the inset QIII(1) terrace tilt to the south for a distance of ~1 km. We interpret the back-tilting of the terrace in the hanging wall as the result of rotation by a curved fault. The footwall tilt is due to either footwall fault-related folding of the South Kochkor fault or a gradual change in dip of the Akchop Hills fault underlying the terraces.

We calculate a slip rate using the 26 ± 3 m difference in height between six surveyed points in the hanging wall and one surveyed point in the footwall that is closest to the fault scarp. The active trace of the South Kochkor fault is not exposed at the range front. An older trace exposed in the hanging wall dips ~45ºS, and juxtaposes granite against Neogene sandstone [*Sadybakasov*, 1972]. Based on the map pattern of the fault, which suggests a moderate to steep dip, the dip is represented by a trapezoidal probability distribution with a maximum likelihood of 30-70ºS (Appendix C). The slip rate of the South Kochkor fault is 0.2 +0.9/-0.03 mm/yr (Figure 10b).

5.3. Kadjerty and Central Naryn faults, Naryn basin

The Naryn Valley occupies one of the largest intermontane basins in the Kyrgyz Tien Shan and contains abundant evidence for Quaternary shortening [*Burbank et al.*, 1999; *Makarov*, 1977; *Sadybakasov*, 1990; *Schulz*, 1948]. Much of the late Quaternary deformation is associated with two south-vergent thrust faults that reach the surface in the northeastern and north-central portions of the basin (Figures 2 and 11). Both the Central Naryn and Kadjerty faults are continuous for ~100 km, with the mapped trace of the Central Naryn fault extending farther east, and the Kadjerty fault extending farther west.

The Akchatash fault and associated folds separate the northern margin of Naryn basin from the Moldo-Too Range [*Makarov*, 1977] (Figure 11). Late Quaternary terraces that cross the boundary between basin and range do not seem to be deformed. In several locations this fault cuts a Plio-Pleistocene conglomerate unit, but in others anticlinal folding of the pre-orogenic erosion surface and an unconformable contact between pre-Cenozoic "basement" and Cenozoic strata mark the basin boundary. The anticlinal folding at the basin margin seems to indicate the transfer of fault slip from a north-dipping crustal ramp underlying the Moldo-Too to the gently north-dipping Kadjerty and Central Naryn faults that penetrate the northern Naryn basin. We have calculated the slip rates for the Kadjerty and Central Naryn faults along the south flowing Kadjerty River, a tributary to the west flowing Naryn River.

5.3.1. Kadjerty fault

The Kadjerty fault crosses several nested terraces in the Kadjerty River valley, ~7 km south of the range front (Figures 11b and 12). On the east side of the Kadjerty River, the fault cuts as many as five terrace levels by progressively greater amounts from a late Holocene terrace adjacent to the modern floodplain to the QII(2) terrace that marks the divide with the adjacent drainage (Figure 12a). Anticlinal folding and the preservation of hanging-wall cut-offs indicate that total fault displacement is less than a few kilometers (Figure 11b).

Profiles across the fault scarp that crosses the broad QIII(2) terrace east of the Kadjerty River show vertical separations from ~8 m at the east end increasing to ~11 m near the west edge of the tread (Figure 11). We calculate the slip rate of the Kadjerty fault using a profile at the west end of the terrace tread that lies close to the adjacent terrace riser to the inset QIV terraces (Figures 11 and 13). Although the fault plane is not exposed in either valley wall of the Kadjerty River, we calculate the fault dip by measuring the scarp locations on the QIII(2) terrace and on the adjacent QIV terrace. Using the average trend of the QIII(2) terrace scarp (N66ºE) and the QIV terrace scarp (N71ºE) to establish the strike of the fault, we calculate a fault dip of 29 ± 5ºN at the QIII(2)/QIV riser. The uncertainty in the dip incorporates the 5º difference in strike above and below the riser and the uncertainties in the locations of the fault within the scarps on the upper and lower terrace surfaces. A decrease in terrace height north of the profile in Figure 13 indicates that the fault dip decreases to ~10°N at depth.

Three radiocarbon analyses on detrital charcoal constrain the timing of river incision, floodplain abandonment, and formation of the QIII(2) terrace along the Kadjerty River (Figures 3, 11 and 12; Table 1). The weighted age distribution of the three samples results in a 13.7-15.3 x 10^3 cal yr B.P. age range for the QIII(2) terrace gravel contact (Appendix C). Using the parameters outlined above, Equations A3-A6 yield a slip rate of 1.5 +0.4/-0.3 mm/yr (Figure 13).

5.3.2. Central Naryn fault

Two splays of the Central Naryn fault that cut QIII terraces west of the Kadjerty River merge into a single fault trace near the west river bank (Figure 11), where a ~40 m-high exposure shows that the Central Naryn fault dips 37 ± 2º N (Figure 12d). A profile of the top of fluvial gravel on the QIII(2) terrace shows a small anticline near the fault scarp and an abrupt bend ~750 m north of the scarp. North of the bend, the terrace slopes 0.9º S, similar to the 0.9º S slope of the modern river (Figure 14a). South of the bend the terrace surface is sub-horizontal, implying a back-rotation that we attribute to changes in underlying fault dip. The change in terrace height, with the assumption of constant fault dip and the recognized ~37° N dip at the surface, is consistent with a fault dip of ~12° N at depth.

To evaluate slip rate, we determine the vertical separation of the terrace close to the scarp, confining our calculation to surveyed points in the hanging wall that are within 100 m of the fault exposure (Figure 14b). The vertical separation of the QIII(2) terrace is 20.6 ± 1.0 m. A point surveyed on the fault plane constrains the location of the fault (point P in Appendix A). Using the known fault location, the 37 ± 2º fault dip, and the age distribution described in Appendix C, the rate of dip slip for the Central Naryn fault is 2.3 +0.3/-0.4 mm/yr (Figure 14b).

5.4. Oinak-Djar fault, At-Bashi basin

The south-vergent Oinak-Djar fault ("Quaternary fault" of *Makarov* [1977]) appears to accommodate most of the late Quaternary shortening across the western and central At-Bashi basin (Figures 2 and 15). For most of its 80-km strike length the fault separates hills composed of steeply dipping Tertiary sediments and large late Quaternary fans (Figure 16).

Although for much of its length a well defined scarp indicates that the Oinak-Djar fault reaches the ground surface, the thrust fault is concealed along its eastern portion as slip is transferred into growth of a fault-propagation fold. Right-stepping en-echelon fold axes in the hanging wall of the fault and deflected drainages indicate a minor component of left-lateral shear to this fault [*Makarov*, 1977] (Figure 15).

We excavated a 20 m-long trench across the Oinak-Djar fault where the fault has offset the head of an alluvial fan repeatedly during the late Quaternary Period (Figures 16 and 17a). Trench-wall exposures reveal four thrust splays that displace a series of colluvial and fluvial deposits (Figure 17a). We correlate two deposits across the fault zone that contain detrital charcoal. The oldest correlative deposit (layer C in Figure 17a) is the lower of two layers of silty sand colluvium that are interstratified with coarse sand and fine gravel alluvium. The younger correlative deposit (layer A in Figure 17a) contains coarse sand and fine gravel alluvium with a laminar silt layer at its base, and is overlain by silty sand colluvium.

We determine the slip rate of the Oinak-Djar fault by measuring vertical separations of layers A and C across the fault zone. In order to restore the anticlinal folding of layers A and C in the hanging wall, we assume that the projected contacts dip 8.4°S, similar to the terrace surface immediately north of the trench (Figure 17b). Vertical separations of layers C and A are 4.2 +0.5/-0.3 m and 4.0 +0.4/-0.3 m, respectively. Radiocarbon ages of detrital charcoal fragments indicate that layer C was deposited ~9.6-10.4 x 10^3 cal yr B.P. and the laminar silt at the base of layer A was deposited ~9.0-9.3 x 10^3 cal yr B.P. (Figure 17a and Table 1). This yields a slip rate of 0.9 ± 0.4 mm/yr for layer C and a 0.9 +0.5/-0.4 mm/yr slip rate for layer A. The pooled slip rate is 0.9 ± 0.3 mm/yr for the Oinak-Djar fault (Figure 17b).

5.5. North and South Kyrkungey faults, Aksay basin

Only two faults appear to have significant late Quaternary slip rates in the eastern Aksay basin. These faults, which we call the North and South Kyrkungey faults, are part of a ~40 km-long system of folded hills that trend about 10 km southeast of and parallel to the southeastern At-Bashi Range front [*Makarov*, 1977] (Figures 2 and 18). Our reconnaissance suggests that this fault system within the Aksay basin is more active than the Northern Aksay fault that defines the northern margin of the basin. Large moraines, formed during the last glacial period, are offset less than one meter by the North Aksay fault. Inset, younger moraines do not appear displaced. The North and South Kyrkungey faults cut alluvial terraces downstream of the moraines, and show signs of recent offset in several locations. Both the North and South Kyrkungey faults appear to dip south, in a direction opposite of the North Aksay fault that marks the southern boundary of the At-Bashi Range. One possibility is that these faults form a basement-involved structural wedge that connects to the south-vergent North Aksay fault at depth [*Narr and Suppe*, 1994]. Our mapping and slip-rate evaluation of the two faults are crude, partly due to limited time in the field at this location and the poor exposure of underlying late Cenozoic strata. Despite the imprecision, the slip rates of these faults are low compared to those discussed above.

5.5.1. North Kyrkungey fault

The North Kyrkungey fault displaces the heads of small Holocene fans and terraces southeast-side up between the Djolbogoshtu River and the Kashkasu River (Figures 18 and 19). Elsewhere along the trace of the fault evidence of recent surface faulting is absent or unclear, suggesting that the fault does not reach the surface in all locations or consists of several short segments, although an aligned row of folds to the northeast indicates that late Quaternary deformation continues along strike. With a hand level, we measured a 1 ± 0.5 m high scarp across a low terrace that lies ~2 m above the present Kashkasu River (Figures 19b,c). The age of the terrace and the dip of the fault are uncertain. Since the offset terrace lies below and between terraces that aggrade to moraines of the last glacial period upstream, we consider it to be postglacial in age, and assume it formed 6-12 ka. The surface trace of the fault has a curved topographic expression that suggests a gentle dip. A trapezoidal probability distribution for the dip, with maximum probability between 20-40ºS (Appendix C), gives a dip slip rate of 0.1 +1.1/-0.07 mm/yr for the North Kyrkungey fault (Figure 19d). Although we saw evidence for recent surface ruptures along the fault trace, small cumulative displacement of less than a few meters across older late Quaternary surfaces (e.g., the terraces in the background of Figure 19b) suggests that the late Quaternary slip rate is low.

5.5.2. South Kyrkungey fault

The South Kyrkungey fault lies 2-3 km south of and parallel to the North Kyrkungey fault (Figure 18). The fault has displaced, southeast-side up, a broad terrace that is between ~40 and 75 m above the modern Kashkasu and Bogoshti-Kakasu rivers (Figure 20a). A profile across the fault scarp shows a vertical separation of 24 ± 5 m (Figure 20b). Numerous gullies along the scarp face are deflected left-laterally about 1-2 m, indicating a component of sinistral slip.

We infer the age of the displaced terrace from stratigraphic relationships and correlation to dated terraces in other intermontane basins. Air photo analysis and field observations show that moraines inferred to be from the last glacial maximum were deposited on top of a terrace located on the east side of the Kashkasu River that is at a similar height to the one we measured. Based on this stratigraphic relationship and the height and prominence of this terrace, and assuming that major terraces aggraded and incised synchronously, we interpret it to be equivalent to the QII(2) terrace dated elsewhere (Figure 3; Table 2), and assign it an age of 141 ± 17 ka. Based on its straight map trace, the fault dips steeply, and we use a trapezoidal probability distribution with maximum likelihood between 30-70º S (Appendix C). The parameters described above yield a rate of dip slip for South Kyrkungey fault of 0.2 +0.9/-0.1 mm/yr (Figure 20b). The eastward continuation of this fault into the Kashkasu River valley does not appear to cut an inset terrace, or interrupt the same low terrace that is cut by the North Kyrkungey fault, supporting the interpretation of a low slip rate.

6. Discussion

We identified eight faults that appear to have the highest late Quaternary slip rates along an approximately north-south transect that crosses the northern two-thirds of the central Tien Shan (Figure 21). The rates of dip-slip faulting on individual faults range from ~0.1 mm/yr to ~2.9 mm/yr, and generally accommodate shortening in a north-south direction. The high slip rates of faults within the intermontane Kochkor and Naryn basins clearly demonstrate that active shortening over the late Quaternary is distributed across the belt, and is not concentrated along the margins, where most historic large-magnitude earthquakes have occurred [e.g., *Molnar and Ghose*, 2000]. The most active faults lie in the major Cenozoic basins, and both the geologic mapping and pattern of terrace deformation indicate that they are active splays of fault systems that dip either north or south beneath five range/basin margins across the belt. The pattern suggests that the upper crust consists of fault-bounded blocks with a spacing of ~35 to 80 km.

We recognize within the range blocks several Cenozoic-active faults that displace the early Cenozoic erosion surface (Figure 2), indicating that deformation does occur within the range-scale “blocks.” Because these faults lie in areas of high topography with actively eroding hillslopes and steep, bedrock-floored channels, late Quaternary deposits and landforms that would easily record recent fault slip are few; quantifying late Quaternary slip rates of these faults, and their contribution to overall mountain belt deformation, is difficult to determine. As an example, although ~200 km of surface rupture occurred during the 1911 M ≈ 8 Chon-Kemin earthquake [*Bogdanovitch et al.*, 1914; *Kuchai*, 1969], landslides and actively aggrading debris fans have covered much of the evidence for prior events along the portion of the fault trace that follows the narrow Chon-Kemin valley [*Delvaux et al.*, in review].

To evaluate the degree to which the faults we identified account for the total crustal shortening across the Kyrgyz central Tien Shan, we converted the calculated fault slip rates to crustal shortening rates (Appendix D), and compared them along a transect line to modern crustal velocities measured by GPS [*Herring et al.*, manuscript in preparation] (Figure 21). As some of our study sites are tens of kilometers away from the transect line, we treat fault slip as constant along strike, recognizing that such an assumption cannot be correct everywhere (for example, the surface traces of the Oinak-Djar and Kyrkungey faults do not appear to extend to the transect line in Figure 21). Where we measured rates of two faults at a particular range-basin boundary, we consider the faults as splays of the same fault zone at depth, and combine their shortening rates.

Cumulative shortening rate plotted against distance and increasing from north to south shows an approximately linear trend across the northern 2/3 of the belt, with a total rate of 11 +2/-1 mm/yr (Figure 22). The cumulative geologic rates and current GPS rates are indistinguishable at a 95% confidence level (Figure 22). Assuming that the total rate across this area has remained constant over the past ~10^5-10^6 years, and that the GPS rates are indicative of far-field convergence rates across the deforming region [cf, *Hager et al.*, 1999], slip on the faults we have studied account for the vast majority of crustal shortening. This result suggests that only minor deformation occurs within the blocks. The faulting and folding that do occur presently within the blocks likely resolve space problems within hanging-wall material deforming differentially across bends of major fault zones within the upper crust [*Narr and Suppe*, 1994].

The distribution of slip rates in Figure 21 and the shortening rate profiles in Figure 22 indicate lower slip rates in the southern region, which also occupies the highest topography and thickest crust [S. Roecker, personal communication, 2000]. There are at least two explanations for the difference in an otherwise consistent strain-rate pattern across the range. The first is that the crust continues to thicken beneath the high region in the south, by either ductile flow or faulting at depth. The second is that the high topography and thick crust are nearing a limit to crustal thickening, and perhaps represent nascent plateau formation. This may be due to the extra work required to further thicken already thick crust compared to work required to thicken areas of lower mean topography, thinner crust, and lesser gravitational potential energy [e.g., *Molnar and Lyon-Caen*, 1988].

Comparison with other regions of convergent deformation distant from plate boundaries is difficult either because other belts are ancient or because strain rate distributions have not been similarly studied. Slip across many blocks of the Rocky Mountain foreland province during the Laramide orogeny appears synchronous during the Late Cretaceous, but slip terminated at different times during the Eocene [*Dickinson et al.*, 1988]. In the Sierras Pampeanas region of Argentina, initiation appears diachronous [*Coughlin et al.*, 1998; *Jordan and Allmendinger*, 1986], although the numerous active range fronts showing evidence for late Quaternary or Holocene faulting indicates a currently distributed strain rate field [*Costa and Vita-Finzi*, 1996; *Hermanns and Strecker*, 1999]. A shared characteristic appears to be the geometry and spacing of deformation, with a block-like pattern of deformation with little deformation internal to the blocks [*Erslev and Rogers*, 1993; *Gries*, 1983; *Hand and Sandiford*, 1999; *Jordan and Allmendinger*, 1986]. This spacing is perhaps related to buckling instabilities within a brittle upper crust [e.g., *Burov et al.*, 1993; *Martinod and Davy*, 1992; 1994].

7. Conclusions

Our results indicate that mountain building in the Central Tien Shan occurs by concurrent slip across several faults that span the width of the mountain belt. Active shortening occurs along the boundaries between major ranges and intermontane basins, although the most active faults penetrate and deform the intermontane basin margins. Slip rates have been rather evenly distributed across the Kyrgyz Tien Shan during late Quaternary time, consistent with present-day geodetic measurements [*Abdrakhmatov et al.*, 1996; *Herring et al.*, manuscript in preparation] and more crudely inferred late Cenozoic rates [*Makarov*, 1977; *Sadybakasov*, 1972; *Tapponnier and Molnar*, 1979]. Distributed shortening by localized slip between blocks of similar dimensions also appears to characterize deformation of other continental regions distant from plate boundaries.

Appendix A. Slip rate calculation for an offset river terrace

We consider the case of a fault that has cut an originally planar river terrace. Our measurements are points surveyed along the terrace surface and across the fault. To calculate the amount of fault slip that has offset the terrace, we rotate and project all field data onto a vertical plane normal to the structural trend. Surveyed points from the river terrace treads define the strain markers for hanging-wall and footwall deformation. Least-squares linear regressions of these points in an x-y coordinate system determine the mean and standard error of both the slope and the intercept of the lines representing the hanging wall ($y_h = m_h x + b_h$) and footwall ($y_f = m_f x + b_f$), where the tangent of the terrace dip, $\tan \alpha = m$ (Figure A1).

We determine fault dip, δ, by direct measurement, by surveying the position of the fault scarp across at least two nested terraces, or by estimation based on geomorphic expression (Appendix C). For parallel strain markers in the hanging wall and footwall, the vertical separation is $v = b_h - b_f$, and the dip-slip component s is

$$s = \frac{v}{\sin\delta + m\cos\delta}$$

or

$$s = \frac{v\cos\alpha}{\sin(\alpha + \delta)}. \qquad \text{(A1)}$$

If the hanging-wall and footwall strain marker surfaces are not parallel ($m_h \neq m_f$), the calculated vertical separation is a function of horizontal distance

$$v(x) = x(m_h - m_f) + b_h - b_f, \tag{A2}$$

and the dip-slip calculation requires a knowledge of the position (or projection) *P(x,y)* of the fault tip onto the scarp (Figure A2). A line fit to the scarp face $y = m_s x + b_s$ contains all possible points *P*. We divide the amount of dip slip into two parts: the distance from the footwall projection up to *P*,

$$s_f = \frac{x(m_s - m_f) + b_s - b_f}{\sin\delta + m_f \cos\delta} \tag{A3}$$

and the distance from the hanging wall down to point *P*,

$$s_h = \frac{x(m_h - m_s) + b_h - b_s}{\sin\delta + m_h \cos\delta}. \tag{A4}$$

Therefore,

$$s = s_f + s_h \; . \tag{A5}$$

Assuming that the terraces have deformed by incremental slip during earthquakes, we incorporate an additional uncertainty in slip rate due to the earthquake cycle [*Sieh and Jahns*, 1984]. Paleoseismic data from trench excavations suggests that major ground-rupturing earthquakes on individual faults recur on the order of one to several (1-5) thousands of years [*Rubin et al.*, 1999]. Hence, deformation of a ~15 ka terrace may have occurred during a few earthquakes. To incorporate uncertainty due to the earthquake cycle, we follow *Lavé and Avouac* [2000] and consider that some elastically stored slip Δs may be presently stored, and some elastically stored slip Δs_o may have been stored at the time of terrace formation. In the Monte Carlo simulations, we add the additional terms Δs - Δs_o to *s* (Appendix C).

Datable material collected from fine-grained sediments covering river terrace gravel or from within a confined deposit offset by a fault provides a measure of the time since formation of the strain marker, t. Hence, the dip slip rate, u, for the case of an offset terrace is:

$$u = \frac{s + \Delta s - \Delta s_o}{t}. \qquad \text{(A6)}$$

Appendix B. Measuring slip rate with fault-bend folding of terraces

We consider the case of a terrace that has been deformed by fault-related folding, where the terraces surface is folded in the hanging wall of the fault but is buried by aggradation in the footwall. A valid geometric and kinematic interpretation of the fault-related folding must be compatible with both the terrace deformation and the underlying geologic structure. We combine measurements of deformed strata that underlie terrace treads with surveyed profiles of terrace surfaces to calculate the amount of fault slip since the terrace was formed. Our observations in the field indicate that attitudes of Tertiary beds are well approximated by kink-style geometry, with sections of relatively constant dip separated by narrow axial surfaces. The first step is to rotate a profile in the vertical plane so that axes are parallel and perpendicular to the present river gradient, which is assumed to be close to the original river gradient at the time of terrace formation. We assume that the angle between the river gradient and the fault, δ, and the angle between the river gradient and the hanging wall strata, α, are equal (i.e., no hanging-wall cut-off). Fault-bend fold theory [*Suppe*, 1983] predicts the deformation of an unconformity (i.e., terrace) above a growing fault-bend fold [*Thompson et al.*, 1999] (Figure B1). We compare the measured terrace profile to predictions of the deformation of a river terrace due to slip on an inferred fault.

The difference in height of a terrace across a fold backlimb (h_1-h_2) and the fault dip beneath the terrace sections after and before the fault bend (δ_1~α_1 and δ_2~α_2) constrain the amount of fault dip slip s (Figure B1):

$$s = \frac{h_1 - h_2}{\sin\delta_1 - \sin\delta_2}. \qquad \text{(B1)}$$

A test of the fold model is possible from measurements of the dip of the terrace backlimb, ψ, defined in Figure B1, which is predicted by applying fault-bend fold theory to an unconformity:

$$\psi = \arctan\left(\frac{\sin\delta_1 - \sin\delta_2}{\cos\delta_1 + \sin\delta_2 \tan\left(\frac{\alpha_1 + \alpha_2}{2}\right)}\right). \qquad \text{(B2)}$$

The 95% confidence minimum and maximum, and the most probable value of slip rate are calculated using equation A6 and the Monte Carlo simulations described in Appendix C.

The fold-growth analysis also predicts the change in river height since initial floodplain abandonment and terrace formation. The equation for a change in river height relative to the modern river, h_r, is

$$h_r = s^*\sin\alpha_1 - h_1. \qquad \text{(B3)}$$

Our calculations indicate that h_r, and rates of river aggradation h_r/t, can be significant and variable through time, and that estimates of slip rate or ages of undated terraces based only on terrace height above the modern river may be significantly in error.

Appendix C: Representation and calculation of uncertainties

We use Monte Carlo simulations to calculate uncertainties in slip rate. Ten thousand calculations sample a variety of probability distributions that represent uncertainties for each variable (Figure C1). Frequency peaks define the most probable slip rate, and the 2.5% and 97.5% tails in the histograms bound the 95% confidence limits. These simulations take into account the standard errors associated with linear regressions of profile data (*m, b*), errors associated with measuring fault dip (δ), fault location across a scarp ($P(x,y)$), elastic strain accumulated during the earthquake cycle (Δs and Δs_o), and age (t),. Because the shape of the probability density function for many of the measured parameters is complex (e.g., calibrated age distributions of charcoal samples [*Stuiver et al.*, 1998]) or poorly known (e.g., $P(x,y)$), we use several methods to describe uncertainty distributions. For parameters characterized by a measurable mean and standard error (e.g., m and b), we use normal distributions. For parameters with either complicated (e.g., t) or otherwise asymmetric uncertainties, we use discrete probability distributions, which we will explain below.

The equations for calculating slip rate assume that strain markers that are offset by a fault (Appendix A) or that mark growth of a fold in a hanging wall (Appendix B) are planar surfaces. For deformed terraces, linear regressions of surveyed points oriented normal to fault strike provide a mean and standard error for m and b that define the strain markers. In trench exposures, linear regressions of points that are digitized from trench logs define mean and standard error of displaced strata.

Fault dip is either calculated by direct measurement, determined by cross-section geometry, or estimated based on geomorphic expression. For instances where the fault surface can be measured directly from natural and artificial exposures with an inclinometer or from a trench log, a "best estimate" and estimated ~95% confidence values are considered to equal a mean and 2σ with a normally distributed probability distribution if the best estimate is symmetric about the uncertainty. If uncertainties are asymmetric about a best estimate, we use a triangular distribution with the best estimate having the maximum probability, and diminishing probabilities to the ~95% minimum and maximum values [*Humphreys and Weldon*, 1994].

In cases for which a fault is not directly exposed, surveying of the trends of a fault that cuts successive inset terraces allows calculation of planar fault geometry with a probability distribution based on linear regression of surveyed points.

For faults that are blind or buried, and fault slip is manifested by growth of a fold, fault dip is derived from measurements of strata exposed within the hanging wall, based on fault-related fold models of fold growth [*Suppe*, 1983]. In the two cases we show in this paper, we use cross-section solutions that assume faults locally cut parallel to hanging-wall strata [e.g., *Lavé and Avouac*, 2000], and the measurements of hanging-wall strata (α, the angle between the strata and the modern river profile) determine the mean and standard deviation of the fault angle (δ, the angle between the fault and the modern river profile).

In cases for which direct measurement of the fault dip was not possible or hanging wall strata were unexposed or ambiguously related to fault orientation, we estimate fault dip based on topographic expression and by analogy with other faults in similar physiographic settings.

Faults that appear to dip steeply are represented by a trapezoidal probability distribution, with an equal and maximum likelihood between 30-70°, and probabilities diminishing linearly to zero at 0° and 90° dips. Faults that appear to dip shallowly have a trapezoidal distribution with equal and maximum likelihood between 20-40°, and probabilities diminishing linearly to zero at 0° and 90° dips.

If the position (or projection) of the fault within the fault scarp ($P(x,y)$) is unknown, we use a trapezoidal probability distribution to represent x in equations A2-A4. Based on examples of exposed thrust faults in our study area and reviews in the literature [*Carver and McCalpin*, 1996], we give a maximum probability to a fault that projects to 1/3 - 1/2 the distance along the scarp face measured from the base of the fault scarp, and a likelihood diminishing to zero at the top and base of the scarp.

For uncertainties associated with the earthquake cycle, we follow *Lavé and Avouac* [2000] and consider that some elastically stored slip Δs may be presently stored, and some elastically stored slip Δs_o may have been stored at the time of terrace formation. In the Monte Carlo simulations (Appendix C) we add the additional term $\Delta s - \Delta s_o$ to s and assume that the values Δs and Δs_o range uniformly between zero and a maximum of 5 m, a value slightly greater than the maximum 4.2 m surface fault slip caused by the 1992 *Ms* 7.3 Suusamyr earthquake [*Ghose et al.*, 1997]. In instances where a scarp appears to have formed in a single earthquake, we limit Δs and Δs_o to vary between zero and the calculated value of s.

We use a variety of methods to generate probability distributions for the ages of strain markers in our slip-rate calculations. Because of fluctuations in cosmogenically produced atmospheric ^{14}C through time, radiocarbon ages of organic material that incorporate atmospheric ^{14}C require calibration in order to be converted to the calendric time scale [*Stuiver and Reimer*, 1986; *Stuiver et al.*, 1998]. Calibration programs [*Ramsey*, 1995; *Stuiver and Reimer*, 1986] use published calibration curves [*Stuiver et al.*, 1998] to convert radiocarbon ages and analytical uncertainties to calibrated (approximately calendric) dates with discrete probability distributions (Figure 3, Table 1). Although detrital charcoal within a deposit has an inherited age that is older than the age of deposition, we presume that this inherited age is small compared to the analytical uncertainty of the radiocarbon age (typically 40-80 ^{14}C yr for our samples, see Table 1). In cases where the age of a deposit is constrained by a single radiocarbon sample (e.g., a charcoal sample collected from an offset layer in a trench), we use the discrete probability distribution of the calibrated radiocarbon age in our slip-rate calculations (Figure C1c). If more than one sample is collected from a deposit, a significance test determines whether the pooled mean radiocarbon age is calibrated to determine the unit age [*Stuiver and Reimer*, 1986], or a combined and reweighted probability distribution is used for the age [e.g., *Biasi and Weldon*, 1994].

In cases for which the age of a contact is desired (e.g., the geologic event that is the paleo-river incision and terrace formation, approximately represented by the contact between river gravel and overlying fine-grained sediments), and samples collected from above and below the contact constrain its age, the extra condition of stratigraphic order is used to re-weight the calibrated age distributions to generate a discrete probability distribution for the age of the contact [*Biasi and Weldon*, 1994; *Ramsey*, 1998]. For example, three radiocarbon dates on detrital charcoal constrain the age of river incision, floodplain abandonment, and formation of the QIII(2) terrace along the Kadjerty River (Figure 3, Table 1). The pooled mean radiocarbon age of two charcoal samples collected in sandy silt 10 and 30 cm above the upper gravel contact in a gully exposure ~2 km south of the fault scarp (Figures 11 and 12c) yields a calibrated radiocarbon age of 13.5-14.1 x 10^3 cal yr B.P. (Table 1). A charcoal sample collected 10 cm below the upper gravel contact in an exposure across the fault scarp (Figures 11 and 12b) has an age of ~14.1-15.4 x 10^3 yr cal yr B.P. (Table 1). Assuming that the charcoal samples closely date the deposits (i.e., they have an inherited age that is negligible compared to the analytical uncertainty in their age measurement), and that the contact between the gravel and overlying sandy silt represents the incision of the paleo-river and formation of the QIII(2) terrace, the extra condition of stratigraphic superposition changes the probability distribution of the age of the contact (Figure C2).

Although the TL and IRSL ages of the QII(2) terraces have large uncertainties (Figure 3 and Table 2), and the samples collected from fine-grained sediments overlying river gravel represent minimum ages for the terraces, statistical tests of significance [*Ward and Wilson*, 1978] cannot reject the hypothesis that all of the QII(2) ages come from the same population (test statistic T = 2.51; $\chi^2(0.05) = 7.81$). To increase the precision for the slip-rate calculations based on deformed QII(2) terraces, we use the pooled mean age (140.7 ka) and standard deviation (square root of the variance of the pooled ages, 8.5 ka) of the statistically similar TL/IRSL analyses. In the text we report the mean and ~95% confidence interval as 141 ± 17 ka.

Additional support for using the pooled age from minimum ages of the terraces comes from the radiocarbon age results from QIII(2) and QIII(3) terraces. At the 95% confidence interval, the calibrated ages of the eight charcoal samples that constrain the age of floodplain abandonment and terrace formation overlap (Figure 3 and Table 1). The similarity between minimum limiting ages (samples collected from fine-grained sediments overlying river gravel) and the maximum limiting age for the QIII(2) terrace (sample 98/KadjQ3tr/11, collected 10 cm below the travel contact) indicates that paleo-river incision and formation of the QIII(2) and QIII(3) terraces occurred rapidly. Since the QII(2) terrace and the QIII(2) terraces are defined based on their prominent morphology in river valleys (broad terrace treads with narrower terraces preserved in the risers), and their ages correlate closely with similar periods of global climate change (major glacial/interglacial transitions documented by *Imbrie et al*. [1984] and refined more recently by others), it is reasonable to suppose that their processes of formation were similar, and that incision and abandonment of the floodplain to form the QII(2) terrace occurred rapidly.

For the study sites where we do not have local age control (e.g., in the southernmost Aksay basin), we use geomorphic criteria and correlation to estimate terrace ages. For terraces mapped as QII(2) or QIII(2) [*Abdrakhmatov*, unpublished data], we use the pooled mean age of the terrace determined at other sites. For other terraces we estimate an age distribution based on the stratigraphic relationship between the terrace and other terraces or landforms.

Appendix D: Converting slip rates to geologic shortening rates

To convert the slip rate on a fault to its contribution to the shortening rate across the region, we cannot assume that slip on the crustal-scale ramp equals that on the fault segments at shallow crustal depths (Figure D1). Most of the faults that we have examined in this study dip ~ 20-40° at the surface and appear to flatten to dips of ~ 5-20° at depths of less than a few kilometers, within Tertiary sedimentary rock (e.g., Figure 9 and B1). Fault-bend fold theory predicts that, in layered strata at least, where shear can occur parallel to bedding, slip on consecutive fault segments with dips that steepen upwards remains approximately constant (see p. 699 in *Suppe* [1983]).

The shallow faults that lie at a few kilometers depth appear to intersect more steeply dipping faults that underlie the mountain ranges and involve much of the previously deformed basement rock in the upper crust [e.g., *Avouac et al.*, 1993; *Burchfiel et al.*, 1999]. Strain must occur in the hanging wall to absorb the movement in different directions of the portions adjacent to segments with different dips. The fraction of slip, s, transferred from a deeper, steeper fault (dip = δ_1) to a more gently dipping, shallower fault (dip = δ_2) is approximately equal to $\cos\delta_1/\cos\delta_2$ (see the Fault-bend Anticline example in *Narr and Suppe* [1994], p. 814, and Figure D1). Where deformation of the hanging wall occurs only by shear on vertical planes, the approximate equality becomes exact. In the case where shear occurs on planes with a non-zero angle β, the equation for the shortening rate u_h, derived in Figure D1, is

$$u_h = \frac{u_2 \cos\delta_2 (1 - \tan\delta_2 \tan\beta_3)}{1 - \tan\delta_1 \tan\beta_3}. \qquad \text{(D1)}$$

Values of u_2 are derived from our slip calculations, and we estimate (or infer) δ_2 from cross-sections and folds in terrace profiles. Where we have no mapping constraints on δ_2, we allow

δ_2 to vary between the dip of the fault measured or estimated at the surface in our slip rate calculations and 0°. For δ_1 we assume that crustal scale ramps dip between δ_2 and 55° (the maximum dip of the intermontane 1992 Suusamyr earthquake [*Mellors et al.*, 1997]), and we assign β_3 values between 0-5°.

We compare our late Quaternary shortening rates to the north component of GPS shortening rates [*Herring et al.*, manuscript in preparation]. In order to resolve geologic shortening into its north-south component, we must also calculate the N-S component of slip on faults that do not strike normal to this direction (Figure 21). Simple end-member cases are to assume pure dip slip on each fault (N-S component ≤ calculated dip slip), or to assume that oblique slip occurs such that maximum shortening is oriented N-S (N-S component ≥ calculated dip slip). We incorporate this uncertainty by defining ϕ as the angle between the strike-normal direction of the fault and north (Figure D1b) and assuming:

$$u'_h \cos \phi \leq u'_{hns} \leq u'_h / \cos \phi. \qquad \text{(D2)}$$

Acknowledgements

The scientific station IVTAN, under the leadership of G. Schletchkov and the late Yu. A. Trapeznikov, provided excellent logistical support in the field. We thank K. Armstrong, M. Bullen, D. Burbank, K. Fengler, J. Lavé, K. McLean, M. Miller, K. Weberling, and C. Whitehill for help in the field, and Atyr Abdrakhmatov for excellent cooking. T. Herring and B. Hager provided GPS velocities prior to publication. This work was supported in part by NSF research grant EAR 96-14412, and by grants from the Geological Society of America, American Association of Petroleum Geologists, and the University of Washington Department of Earth and Space Sciences to Thompson.

REFERENCES:

Abdrakhmatov, K.E., S. Thompson, R. Weldon, D. Delvaux, and J. Klerkx, Active faults of Tien-Shan (in Russian), *Science and New Technology (Nauka i novye tehnologyi)*, in press.

Abdrakhmatov, K.Y., *Quaternary tectonics of the Chu basin* (in Russian), 120 pp., Ilim, Frunze, Kyrgyzstan, 1988.

Abdrakhmatov, K.Y., S.A. Aldazhanov, B.H. Hager, M.W. Hamburger, T.A. Herring, K.B. Kalabaev, V.I. Makarov, P. Molnar, S.V. Panasyuk, M.T. Prilepin, R.E. Reilinger, I.S. Sadybakasov, B.J. Souter, Y.A. Trapeznikov, V.Y. Tsurkov, and A.V. Zubovich, Relatively recent construction of the Tien Shan inferred from GPS measurements of present-day crustal deformation rates, *Nature*, *384*, 450-453, 1996.

Aitken, M.J., *Thermoluminescence dating*, 359 pp., Academic Press, London, 1985.

Aitken, M.J., *Introduction to Optical Dating*, 256 pp., Oxford University Press, Oxford, 1998.

Arrowsmith, J.R., and M.R. Strecker, Seismotectonic range-front segmentation and mountain-belt growth in the Pamir-Alai region, Kyrgyzstan (India-Eurasia collision zone), *Geological Society of America Bulletin*, *111*, 1665-1683, 1999.

Avouac, J.P., P. Tapponnier, M. Bai, H. You, and G. Wang, Active thrusting and folding along the northern Tien Shan and late Cenozoic rotation of the Tarim relative to Dzungaria and Kazakhstan, *Journal of Geophysical Research 98*, 6755-6804, 1993.

Bally, A.W., L. Burbi, C. Cooper, and R. Ghelardoni, Balanced sections and seismic reflection profiles across the central Apennines, *Mem. Soc. Geol. It.*, *35*, 257-310, 1986.

Benedetti, L., P. Tapponnier, G.C.P. King, B. Meyer, and I. Manighetti, Growth folding and active thrusting in the Montello region, Veneto, northern Italy, *Journal of Geophysical Research*, *105*, 739-766, 2000.

Berger, G.W., Dating Quaternary events by luminescence, in *Dating Quaternary Sediments*, edited by D.J. Easterbrook, pp. 13-50, Geological Society of America, Boulder, 1988.

Berger, G.W., Effectiveness of natural zeroing of the thermoluminescence in sediments, *Journal of Geophysical Research*, *95*, 12,375-12,397, 1990.

Berger, G.W., R.A. Lockhart, and J. Kuo, Regression and error analysis applied to the dose-response curves in thermoluminescence dating, *Nuclear Tracks and Radiation Measurements*, *13*, 177-184, 1987.

Biasi, G.P., and R.J. Weldon, Quantitative refinement of calibrated 14C distributions, *Quaternary Research*, *41*, 1-18, 1994.

Bogdanovitch, K.I., I.M. Kark, B.Y. Korolkov, and D.I. Mushketov, *The Earthquake in the Northern Districts of the Tien Shan, 22 December 1910 (4 January 1911)* (in Russian), Commission of the Geology Committee, St. Petersburg, 1914.

Boyer, S.E., Geometric evidence for synchronous thrusting in the southern Alberta and northwest Montana thrust belts, in *Thrust Tectonics*, edited by K.R. McClay, pp. 377-390, Chapman & Hall, London, 1992.

Boyer, S.E., and D. Elliott, Thrust Systems, *American Association of Petroleum Geologists*, *66*, 1196-1230, 1982.

Brown, E.T., D.L. Bourles, B.C. Burchfiel, Q. Deng, J. Li, P. Molnar, G.M. Raisbeck, and F. Yiou, Estimation of slip rates in the southern Tien Shan using cosmic ray exposure dates of abandoned alluvial fans, *Geological Society of America Bulletin*, *110*, 377-386, 1998.

Bullen, M., D. Burbank, and others, *Geology*, in review.

Burbank, D.W., J.K. McLean, M. Bullen, K.Y. Abdrakhmatov, and M.M. Miller, Partitioning of intermontane basins by thrust-related folding, Tien Shan, Kyrgyzstan, *Basin Research*, *11*, 75-92, 1999.

Burchfiel, B.C., E.T. Brown, D. Qidong, F. Xianyue, L. Jun, P. Molnar, S. Jianbang, W. Zhangming, and Y. Huichuan, Crustal shortening on the margins of the Tien Shan, Xinjiang, China, *International Geology Review*, *41*, 665-700, 1999.

Burov, E.B., L.I. Lobkovsky, S. Cloetingh, and A.M. Nikishin, Continental lithosphere folding in Central Asia (Part II): constraints from gravity and topography, *Tectonophysics*, *226*, 73-87, 1993.

Burtman, V.S., *The Talaso-Ferghana strike-slip rault* (in Russian), 143 pp., Nauka, Moscow, 1964.

Burtman, V.S., Structural geology of Variscan Tien Shan, USSR, *American Journal of Science. Vol*, *275-a*, 157-186, 1975.

Burtman, V.S., S.F. Skobelev, and P. Molnar, Late Cenozoic slip on the Talas-Ferghana Fault, the Tien Shan, Central Asia, *Geological Society of America Bulletin*, *108*, 1004-1021, 1996.

Butler, R.W.H., Thrust tectonics, deep structure and crustal subduction in the Alps and Himalayas, *Journal of the Geological Society of London*, *143*, 857-873, 1986.

Carver, G.A., and J.P. McCalpin, Paleoseismology of compressional tectonic environments, in *Paleoseismology*, edited by J.P. McCalpin, pp. 183-270, Academic Press, New York-London-Toronto, 1996.

Chediya, O.K., *Morphology and neotectonics of the Tien Shan* (in Russian), 313 pp., Ilim, Frunze (Bishkek), 1986.

Cobbold, P.R., E. Sadybakasov, and J.C. Thomas, Cenozoic transpression and basin development, Kyrghyz Tien Shan, Central Asia, in *Geodynamic Evolution of Sedimentary Basins, International Symposium*, edited by N.E. F. Roure, V.S. Shein, I. Skvortsov, pp. 181-202, Technip, Paris, 1994.

Cook, F.A., D.S. Albaugh, L.D. Brown, S. Kaufman, J.E. Oliver, and R.D.J. Hatcher, Thin-skinned tectonics in the crystalline southern Appalachians; COCORP seismic-reflection profiling of the Blue Ridge and Piedmont, *Geology*, *7*, 563-567, 1979.

Costa, C.H., and C. Vita-Finzi, Late Holocene faulting in the Southeast Sierras Pampeanas of Argentina, *Geology*, *24*, 1127-1130, 1996.

Coughlin, T.J., P.B. O'Sullivan, B.P. Kohn, and R.J. Holcombe, Apatite fission-track thermochronology of the Sierras Pampeanas, central western Argentina; implications for the mechanism of plateau uplift in the Andes, *Geology*, *26*, 999-1002, 1998.

Dahlen, F.A., Noncohesive critical Coulomb wedges: An exact solution, *Journal of Geophysical Research*, *89*, 10125-10133, 1984.

Dahlstrom, C.D.A., Structural geology in the eastern margin of the Canadian Rocky Mountains, *Bulletin of Canadian Petroleum Geology*, *18*, 332-406, 1970.

Davis, D., J. Suppe, and F.A. Dahlen, Mechanics of fold-and-thrust belts and accretionary wedges, *Journal of Geophysical Research*, *88*, 1153-1172, 1983.

Delvaux, D., K.Y. Abdrakhmatov, and J. Klerx, *Russian geology and geophysics*, in review.

DeMets, C., R.G. Gordon, D.F. Argus, and S. Stein, Effect of recent revisions to the geomagnetic reversal time scale on estimates of current plate motions, *Geophysical Research Letters*, *21*, 2191-2194, 1994.

Dickinson, W.R., M.A. Klute, M.J. Hayes, S.U. Janecke, E.R. Lundin, M.A. McKittrick, and M.D. Olivares, Paleogeographic and paleotectonic setting of Laramide sedimentary basins in the central Rocky Mountain region, *Geological Society of America Bulletin*, *100*, 1023-1039, 1988.

Erslev, E.A., and J.L. Rogers, Basement-cover geometry of Laramide fault-propagation folds, in *Laramide basement deformation in the Rocky Mountain foreland of the Western United States.*, edited by C.J. Schmidt, R.B. Chase, and E.A. Erslev, pp. 125-146, Geological Society of America, Boulder, CO, United States, 1993.

Fairbanks, R.G., A 17,000 year glacio-eustatic sea level record: influence of glacial melting rates on the Younger Dryas event and deep-ocean circulation, *Nature*, *345*, 637-642, 1989.

Fedorovich, B.A., *Data of Geology and Geochemistry of the Tien Shan* (in Russian), 243 pp., 1935.

Ghose, S., M.W. Hamburger, and C. Ammon, Source parameters of moderate-size earthquakes in the Tien Shan, Central Asia from regional movement tensor inversion, *Geophysical Research Letters*, *25*, 3181-3184, 1998.

Ghose, S., R.J. Mellors, A.M. Korjenkov, M.W. Hamburger, T.L. Pavlis, G.L. Pavlis, M. Omuraliev, E. Mamyrov, and A.R. Muraliev, The $M_s = 7.3$ 1992 Suusamyr, Kyrgyzstan, earthquake in the Tien Shan; 2, Aftershock focal mechanisms and surface deformation, *Bulletin of the Seismological Society of America*, *87*, 23-38, 1997.

Gillespie, A.R., and P. Molnar, Asynchronous maximum advances of mountain and continental glaciers, *Reviews of Geophysics*, *33*, 311-364, 1995.

Gries, R., Oil and gas prospecting beneath Precambrian of foreland thrust plates in Rocky Mountains, *American Association of Petroleum Geologists Bulletin*, *67*, 1-28, 1983.

Grigorienko, P.G., The main features of geological development of Krygyz Tien Shan during the Quaternary Period (in Russian), in *Materials about Cenozoic Geology and the Newest tectonic of the Tien Shan*, Ilim, Frunze, 1970.

Hager, B.H., G.A. Lyzenga, A. Donnellan, and D. Danan, Reconciling rapid strain accumulation with deep seismogenic fault planes in the Ventura basin, California, *Journal of Geophysical Research*, *104*, 25,207-25,219, 1999.

Hand, M., and M. Sandiford, Intraplate deformation in central Australia, the link between subsidence and fault reactivation, *Tectonophysics*, *305*, 121-140, 1999.

Henderson, G.M., and N.C. Slowey, Evidence from U-Th dating against Northern Hemisphere forcing of the penultimate deglaciation, *Nature*, *404*, 61-66, 2000.

Hermanns, R.L., and M.R. Strecker, Structural and lithological controls on large Quaternary rock avalanches (sturzstroms) in arid northwestern Argentina, *Geological Society of America Bulletin*, *111*, 934-948, 1999.

Herring, T.A., B. Hager, and B. Meade,,, manuscript in preparation.

Holt, W.E., R.N. Chamot, X. Le-Pichon, A.J. Haines, T.B. Shen, and J. Ren, Velocity field in Asia inferred from Quaternary fault slip rates and Global Positioning System observations., *Journal of Geophysical Research*, *105*, 19,185-19,209, 2000.

Humphreys, E.D., and R.J.I. Weldon, Deformation across the western United States; a local estimate of Pacific-North America transform deformation, *Journal of Geophysical Research*, *99*, 19975-20010, 1994.

Ikeda, Y., Thrust-front migration and its mechanism; evolution of intraplate thrust fault system, *Bulletin of the Department of Geography, University of Tokyo*, *15*, 125-159, 1983.

Imbrie, J., J.D. Hays, D.G. Martinson, A. McIntyre, A.C. Mix, J.J. Morley, N.G. Pisias, W.L. Prell, and N.J. Shackleton, The orbital of Pleistocene climate: Support from a revised chronology of the marine 18-O record, in *Milankovitch and Climate*, edited by A.L.E.A. Berger, pp. 269-305, Dordrecht, Reidel, 1984.

Jordan, T.E., and R.W. Allmendinger, The Sierras Pampeanas of Argentina; a modern analogue of Rocky Mountain foreland deformation, *American Journal of Science*, *286*, 737-764, 1986.

Knauf, V.I., Tectonic zoning of Northern Kyrgyzia (in Russian), *Geotectonica*, *5*, 1976.

Koyi, H.A., K. Hessami, and A. Teixell, Epicenter distribution and magnitude of earthquakes in fold-thrust belts: insights from sandbox models, *Geophysical Research Letters*, *27*, 273-276, 2000.

Kuchai, V.K., Results of repeated examination of the remaining deformation in the pleistoseist of the Kebin earthquake (in Russian), *Geologia y Geofizika*, 101-108, 1969.

Lavé, J., and J.P. Avouac, Active folding of fluvial terraces across the Siwaliks Hills, Himalayas of central Nepal, *Journal of Geophysical Research*, *105*, 5735-5770, 2000.

Le Fort, P., Himalayas: the collided range. Present knowledge of the continental arc., *American Journal of Science*, *275-A*, 1-44, 1975.

Makarov, V.I., *New tectonic structures of the Central Tien Shan* (in Russian), 171 pp., Order of the Red Banner Geology Institute, Akad. Sci., Moscow, 1977.

Martinod, J., and P. Davy, Periodic instabilities during compression or extension of the lithosphere 1. Deformation modes from an analytical perturbation method, *Journal of Geophysical Research*, *97*, 1999-2014, 1992.

Martinod, J., and P. Davy, Periodic instabilities during compression or extension of the lithosphere, 2. Analog experiments, *Journal of Geophysical Research*, *99*, 12057-12069, 1994.

Mattauer, M., Sur le mécanisme de formation de la schistocité dans l'Himalaya, *Earth and Planetary Science Letters*, *18*, 144-154, 1975.

Mellors, R.J., F.L. Vernon, G.L. Pavlis, G.A. Abers, M.W. Hamburger, S. Ghose, and B. Iliasov, The M_s = 7.3 1992 Suusamyr, Kyrgyzstan, earthquake; 1, Constraints on fault geometry and source parameters based on aftershocks and body-wave modeling, *Bulletin of the Seismological Society of America*, *87*, 11-22, 1997.

Molnar, P., E.T. Brown, B.C. Burchfiel, Q. Deng, X. Feng, J. Li, G.M. Raisbeck, J. Shi, Z. Wu, F. Yiou, and H. You, Quaternary climate change and the formation of river terraces across growing anticlines on the north flank of the Tien Shan, China, *Journal of Geology*, *102*, 583-602, 1994.

Molnar, P., and S. Ghose, Seismic Moments of Major Earthquakes and the Rate of Shortening across the Tien Shan, *Geophysical Research Letters*, *27*, 2377-2380, 2000.

Molnar, P., and H. Lyon-Caen, Some simple physical aspects of the support, structure, and evolution of mountain belts, in *Processes in continental lithospheric deformation.*, edited by S.P. Clark, Jr., B.C. Burchfiel, and J. Suppe, pp. 179-207, Geological Society of America, Boulder, CO, United States, 1988.

Molnar, P., and P. Tapponnier, Cenozoic tectonics of Asia; effects of a continental collision, *Science*, *189*, 419-426, 1975.

Mugnier, J.L., S. Guellec, G. Menard, F. Roure, M. Tardy, and P. Viallon, A crustal scale balanced cross-section through the external Alps deduced from the ECORS profile, in *Deep structure of the Alps*, edited by F. Roure, P. Heitzmann, and R. Polino, pp. 203-216, Societe Geologique de France, Paris, 1990.

Narr, W., and J. Suppe, Kinematics of basement-involved compressive structures, *American Journal of Science*, *294*, 802-860, 1994.

Nelson, K.D., and a. others, Partially molten middle crust beneath southern Tibet; synthesis of Project INDEPTH results., *Science*, *274*, 1684-1688, 1996.

Nelson, M.R., R. McCaffrey, and P. Molnar, Source parameters for 11 earthquakes in the Tien Shan, Central Asia, determined by P and SH waveform inversion, *Journal of Geophysical Research*, *92*, 12,629-12,648, 1987.

Ni, J., Contemporary tectonics in the Tien Shan region, *Earth and Planetary Science Letters*, *41*, 347-354, 1978.

Ollerhead, J., D.J. Huntley, and G.W. Berger, Luminescence dating of the Buctouche Spit, New Brunswick, *Canadian Journal of Earth Sciences*, *31*, 523-531, 1994.

Prescott, J.R., and J.T. Hutton, Cosmic ray and gamma ray dosimetry for TL and ESR, *Nuclear Tracks and Radiation Measurements*, *14*, 223-227, 1988.

Ramsey, B.C., Radiocarbon Calibration and Analysis of Stratigraphy: The OxCal Program, *Radiocarbon*, *37*, 425-430, 1995.

Ramsey, C.B., Probability and dating, *Radiocarbon*, *40*, 461-474, 1998.

Rockwell, T.K., E.A. Keller, and G.R. Dembroff, Quaternary rate of folding of the Ventura Avenue Anticline, western Transverse Ranges, Southern California, *Geological Society of America Bulletin*, *100*, 850-858, 1988.

Rodgers, J., Chains of basement uplifts within cratons marginal to orogenic belts, *American Journal of Science*, *287*, 661-692, 1987.

Royse, F.J., M.A. Warner, and D.L. Reese, Thrust belt structural geometry and related stratigraphic problems: Wyoming, Idaho, northern Utah, in *Symposium on Deep*

Drilling Frontiers in Central Rocky Mountains, pp. 41-54, Rocky Mountain Association of Geologists, Denver, 1975.

Rubin, C.M., S. Thompson, K. Abdrakhmatov, and R. Weldon, Thrust fault paleoseismology in an intercontinental tectonic setting, Kyrgyz Tien Shan, central Asia, *Geological Society of America Annual Meeting, Abstracts with Programs*, *31*, 376, 1999.

Sadybakasov, I., *Neotectonics of the central Tien Shan* (in Russian), 117 pp., Ilim, Frunze (Bishkek), 1972.

Sadybakasov, I., *Neotectonics of High Asia* (in Russian), 176 pp., Nauka, Moscow, 1990.

Schulz, S.S., *Analysis of the neotectonics and relief of the Tien Shan* (in Russian), 222 pp., Geografgiz, Moscow, 1948.

Shackleton, N.J., The 100,000-Year Ice-Age Cycle Identified and Found to Lag Temperature, Carbon Dioxide, and Orbital Eccentricity, *Science*, *289*, 1897-1902, 2000.

Shirokova, Y.I., A detailed study of the stresses and faults at earthquake foci of Central Asia, *Physics of the Solid Earth*, *11*, 707-717, 1974.

Sieh, K.E., and R.H. Jahns, Holocene activity of the San Andreas fault at Wallace Creek, California, *Geological Society of America Bulletin*, *95*, 883-896, 1984.

Stuiver, M., and H.A. Polach, Discussion; reporting of C-14 data, *Radiocarbon*, *19*, 355-363, 1977.

Stuiver, M., and P.J. Reimer, A computer program for radiocarbon age calibration, *Radiocarbon*, *28*, 1022-1030, 1986.

Stuiver, M., P.J. Reimer, E. Bard, J.W. Beck, G.S. Burr, K.A. Hughen, B. Kromer, G. McCormac, J. van der Plicht, and M. Spurk, INTCAL98 radiocarbon age calibration, 24,000-0 cal BP, *Radiocarbon*, *40*, 1041-1083, 1998.

Suppe, J., Geometry and kinematics of fault-bend folding, *American Journal of Science*, *283*, 684-721, 1983.

Suppe, J., G.T. Chou, and S.C. Hook, Rates of folding and faulting determined from growth strata, in *Thrust tectonics.*, edited by K.R. McClay, pp. 105-121, Chapman & Hall, London, United Kingdom, 1992.

Suppe, J., and D.A. Medwedeff, Geometry and kinematics of fault-propagation folding, in *The Hans Laubscher volume.*, edited by P. Jordan, T. Noack, S. Schmid, and D. Bernoulli, pp. 409-454, Birkhaeuser Verlag, Basel, Switzerland, 1990.

Tapponnier, P., and P. Molnar, Active faulting and Cenozoic tectonics of the Tien Shan, Mongolia, and Baykal regions, *Journal of Geophysical Research*, *84*, 3425-3459, 1979.

Tarasov, S.A., *Cenozoic Geology and Neotectonics of the Tien Shan* (in Russian), 211. pp., Ilim, Frunze (Bishkek), 1970.

Thompson, S.C., R.J.I. Weldon, C.M. Rubin, and K.Y. Abdrakhmatov, Late Quaternary river terraces provide kinematic tests for fault-related folding in the Kyrgyz Tien Shan, Central Asia, *Geological Society of America Abstracts with Programs*, *31*, 128, 1999.

Trifonov, V.G., V.I. Makarov, and V.F. Skobelev, The Talaso-Fergana active right-slip fault, *Geotectonics*, *24*, 435-444, 1991.

Ward, G.K., and S.R. Wilson, Procedures for comparing and combining radiocarbon age determinations: a critique, *Archaeometry*, *20*, 19-31, 1978.

Weldon, R.J.I., and K.E. Sieh, Holocene rate of slip and tentative recurrence interval for large earthquakes on the San Andreas Fault, Cajon Pass, Southern California., *Geological Society of America Bulletin*, *96*, 793-812, 1985.

Willett, S.D., Dynamic and kinematic growth and change of a Coulomb wedge, in *Thrust tectonics.*, edited by K.R. McClay, pp. 19-31, Chapman & Hall, London, United Kingdom, 1992.

Willett, S.D., Rheological dependence of extension in wedge models of convergent orogens, *Tectonophysics*, *305*, 419-435, 1999.

Yeats, R.S., and R.J. Lillie, Contemporary tectonics of the Himalayan frontal fault system; folds, blind thrusts and the 1905 Kangra earthquake, in *Characteristics of active faults.*, edited by P.L. Hancock, R.S. Yeats, and D.J. Sanderson, pp. 215-225, Pergamon, Oxford-New York, International, 1991.

Yin, A., S. Nie, P. Craig, T.M. Harrison, F.J. Ryerson, X. Qian, and G. Yang, Late Cenozoic tectonic evolution of the southern Chinese Tien Shan, *Tectonics*, *17*, 1-27, 1998.

Figure captions

Figure 1. Map of the Tien Shan, with shades of gray indicating 1000, 2500, 3500, and 5500 m elevation contours. Approximate boundaries between the Western, Central, and Eastern Tien Shan indicated at the top of the map. Inset map shows the location of the Tien Shan in central Asia, and the box outlines the location of Figure 2.

Figure 2. Preliminary map of active faults and folds in the central Tien Shan plotted with shaded relief. Major intermontane basins and lakes, and selected ranges, are labeled. Thick lines are faults and folds for which we have determined late Quaternary slip rates. The mapped fault and fold traces are from a compilation of satellite and air photo interpretation, field observations, and previous and ongoing studies.

Figure 3. (a) Radiocarbon calibrated age probability distributions for 8 detrital charcoal samples collected from the QIII(2) and QIII(3) river terraces (Table 1). The similar calibrated age ranges suggest that river incision and river terrace formation occurred during a short time interval around 13.5-15.5 x 10^3 cal yr B.P. in several intermontane basins. Calibration plots generated by Oxcal v. 3.5 [*Ramsey*, 1998] based on *Stuiver et al.* [1998]; horizontal bars beneath distributions indicate 67% and 95% confidence intervals. (b) TL and IRSL age distributions (1σ shown) of silt collected from fine-grained sediments covering QII(2) terraces (Table 2). The Djergetal River samples were collected from terrace treads correlated across a fault, and are about 5 km apart. The pooled mean age and standard distribution (square root of variance) of the four ages is shown below, and we use this distribution for the age of the QII(2) terrace. (c) Map of the central Tien Shan, showing sample locations and the river network in the Kyrgyz Republic. Map extent is similar to Figure 2.

Figure 4. (a) Tectonic map of the southern Chu basin, showing major faults, geologic units, and rivers on a shaded-relief digital topographic base. (b) Geologic map of the Alamedin River site, showing terraces, differential GPS survey points, and strikes and dips of Tertiary strata.

Figure 5. (a) Folded terraces of the Alamedin River (river flows to the north). Note the south-dipping QII(2) terrace surface at the south end of the photo (labeled "backlimb"), and inset QIII(2) and QIII(3) terraces (in foreground, under houses and trees). (b) View north along the contact between fluvial gravel and overlying fine-grained deposits (mostly silt) for the QII(2) terrace. (c) Pit excavated for collection of silt for luminescence dating, located ~2.5 m above the contact with fluvial gravel.

Figure 6. (a) Alamedin River profile, showing the deformed QII(2) terrace west of the river, the location and age of the sample collected for luminescence dating, and the apparent dips of Neogene strata exposed below the terraces. Points along the QII(2) terrace are from differential GPS surveying. Points along the Alamedin River are from 1:25,000-scale topographic maps with a 5-m contour interval (gray) and differential GPS (black). We remove the modern river gradient by rotating the data about a horizontal axis so that the x-axis is parallel to the gradient of the river. Apparent dips of strata are similarly rotated. Solid black lines connect surveyed points with continuous exposure; black dashed line indicates our interpretation of a hinge and secondary folding near the top of the hinge and at the northern front. The dashed gray line schematically illustrates the simplification of the geometry of the terrace; this line is constrained by the black points that define the terrace

south and north of the fault bend. We base the slip-rate calculation on this simplified geometry with the values of h_1, h_2, ψ, and δ_1 indicated on the figure. The method for calculating slip rate is described in Appendix B. (b) Histogram showing the predicted value of δ_2, based on equation B2 in Appendix B. The black bars indicate the 95% confidence minimum and maximum, and the most probable value. (c) Histogram showing the predicted amount of dip slip on the Issyk-Ata fault since formation of the QII(2) terrace. (d) Histogram showing the probability distribution of slip rate.

Figure 7. (a) Simplified geologic map of the southern Kochkor basin. The Akchop Hills consist of folded Tertiary strata in the hanging wall of the Akchop Hills fault. (b) Geologic map of the Djuanarik River area, showing nested terraces along the west bank of the Djuanarik River and strikes and dips of underlying strata. Axial surfaces labeled (i), (ii), and (iii) are discussed in the text and in later figures. Surveyed points along the extensive QII(2) terrace constrain our analyses of slip rate for the Akchop Hills fault (profile line A-A') and South Kochkor fault (profile line B-B').

Figure 8. Nested terraces along the west side of the Djuanarik River, Kochkor basin. (a) West view of terraces and Djuanarik River (the river flows north). Arrows indicate locations of Figures b and c. (b) Northwest view of strath terraces; surfaces are labeled. Notice exposed Djuanarik Formation sandstone layers that are folded (Photo by Martin Miller). (c) South view of pit excavated for the collection of silt for luminescence dating on the QII(2) terrace (marked a with white circle). Short arrows mark the contact between fluvial gravel and overlying fine-grained sediments.

Figure 9. (a) Vertically exaggerated river terrace profiles along the Djuanarik River. Profiles were rotated counter clock-wise 0.7° so the horizontal axis would parallel the modern river. Note the progressive limb rotation and kink-band migration recorded by the backlimbs of the QIII(1) and QII(2) terraces off of active axial surfaces (i) and (ii); we infer a back limb for the QIII(2) terrace but did not sample enough points to measure it. The black squares on the QII(2) terrace were used to define the heights of the terrace across axial surface (i). (b) Photo of the backlimb of the Akchop Hills anticline across axial surface (i), showing the QII(2), QIII(1), and QIII(2) terraces. (c) Cross-section across axial surface (i), showing apparent dips of Pliocene Djuanarik Fm. strata and surveyed points along the terraces and modern river. Thick gray lines schematically illustrate dipping strata across the fold. Thin black lines show the predicted terrace profiles assuming that the terraces are deformed by ideal fault-related folding (see Appendix B). Inset box shows the predicted backlimb angle (Equation B2 in Appendix B). Horizontal dashed line shows inferred position of the river at the time of QII(2) terrace formation. (d) Histogram showing slip-rate probability distribution for the Akchop Hills fault based on Equation B1 in Appendix B.

Figure 10. (a) Profile of river terraces across the South Kochkor fault, showing terrace correlation, and folding of the terraces in the hanging wall across axial surface (iii). Black points and horizontal dashed lines indicate the vertical separation used in the slip rate calculation. (b) Histogram showing slip rate calculation for the South Kochkor fault. The 0.2 mm/yr bin contains the minimum slip rate (2.5% tail). Adding another significant digit to the histogram bins yields a 0.17 mm/yr minimum slip rate.

Figure 11. (a) Simplified geologic map of northeastern Naryn basin. The Kadjerty and Central Naryn fault appear to accommodate most of the shortening at the surface across the northern Naryn basin margin. We have evaluated the slip rates of the Kadjerty and Central Naryn faults along the Kadjerty River (box shows area of Figure 11b). (b) Geologic map along the Kadjerty River, showing dips of Tertiary strata, fault and fold traces, and river terraces.

Figure 12. (a) Kadjerty fault scarp cutting nested terraces. Photo is to NE along the scarp. The fault scarp across the QII(2) terrace (in the distance) has a vertical separation of about 60 m; the fault scarp across the QIII(2) terrace to the left has a vertical separation of about 10 m. (b) Gully and trench across the QIII(2) fault scarp near the QII(2) terrace riser exposes terrace gravel and charcoal. Detrital charcoal from the top of the fluvial gravel dates to 14.1-15.4 x 10^3 cal yr B.P. (c) A gully in the QIII(2) terrace between the Kadjerty and Central Naryn faults exposes fluvial gravel and overlying fine-grained sediments. Two detrital charcoal fragments collected above the gravel contact in this exposure date to 13.5-14.1 x 10^3 cal yr B.P. Photo is to the north. (d) Central Naryn fault exposure along the Kadjerty River. View is to the southwest. The exposed fault dips 37 ± 2°N. Neogene strata in the hanging wall dip ~11-15°N. The Kadjerty River flows south along the base of the exposure. Notice thicker accumulation of late Quaternary gravel in the footwall of the fault.

Figure 13. Profile of the QIII(2) terrace across the Kadjerty fault east of the Kadjerty River; location on Figure 11b. Black circles, squares, and diamonds indicate the points used to define the surfaces on the hanging wall, footwall, and scarp face, respectively. Inset histogram shows the slip rate distribution; the most probable slip rate and the 95%

confidence minimum and maximum rates are indicated by the black bars and corresponding values.

Figure 14. (a) Profile of the upper gravel contact of the QIII(2) terrace across the Central Naryn fault near the Kadjerty River; location shown on Figure 11b. The gradient of the QIII(2) terrace and the modern river are similar north of the labeled "hinge," but south of the hinge the terrace surface is subhorizontal, indicating that it has been rotated due to slip on the Central Naryn fault. (b) Close-up view of the profile across the fault scarp, showing the surveyed points used to define the hanging wall and footwall and the dips of those surfaces. A single point surveyed on the exposed fault surface and the measured dip are used to constrain the fault location in the slip-rate calculation. The inset box shows the probability distribution of slip rate from the analysis. Black bars and numbers indicate the 95% confidence limits and the most probable slip rate value.

Figure 15. Simplified geologic map of the western At-Bashi basin. The Oinak-Djar fault marks the boundary between Tertiary strata and late Quaternary deposits, and defines the southeast margin of deformation for the larger structure that separates the Naryn and At-Bashi basins. The Oinak-Djar fault reaches the surface along the western half of the mapped trace; to the east the fault is blind, and the surface expression is a fault-propagation fold with a sharp synclinal axial surface. A trench excavated across the fault (boxed area) provides data to measure slip rate.

Figure 16. (a) View to the north of the Oinak-Djar fault scarp. The fault (between horizontal arrows) separates the hills of steeply dipping Tertiary strata in the hanging wall from the

aggrading alluvial fans in the footwall. The trench site is situated in the eastern part of a wide wash in which multiple terrace levels are progressively displaced by recent slip on the fault. (b) View to the west along the Oinak-Djar fault scarp. The trench and spoil pile are in the foreground. The spoil pile is about 2 m high. The mounds on the fan surface in the middle left of the photo are cultural sites of uncertain age or purpose.

Figure 17. (a) Map of the west wall of the trench across the Oinak-Djar fault. Radiocarbon ages of charcoal samples are in calibrated years before present, and represent ~95% confidence limits (Table 1). We correlate layers A and C across the fault zone and use them to calculate slip rate. (b) Profile of the land surface across the trench. To calculate slip rate (method A), we project layers A and C into the fault zone. The slopes of the projected layers are based on the dip of a terrace surface in the hanging wall, and the dips of the land surface and three layers in the footwall. Changes in layer dip near the fault are interpreted to be drag folding. Histograms show the similar amounts of vertical separation and slip rate. The line in the slip rate histogram shows the pooled mean slip rate and uncertainty by combining the two measurements. (c) Enlargement of the fault zone and data for calculating slip rate using method B. A laminar silt horizon at the base of layer A is used to measure fault slip across the exposed fault zone by adding slip across individual fault strands using simplified traces of the silt contact. Histogram shows the probability distribution of slip rate using method B.

Figure 18. Simplified geologic map of the eastern Aksay basin. The North and South Kyrkungey faults are part of a zone of late Quaternary folds within the northeastern Aksay basin, and appear to accommodate most of the shortening across the basin. Late Quaternary deposits include large amounts of glacial till and outwash; large moraines from the last

glacial period are preserved along the southern At-Bashi Range front and are not offset by more than ~1 m by the North Aksay fault. Locations of photos in Figure 19 and profile line in Figure 20 are shown.

Figure 19. (a) View to the south of the North Kyrkungey fault scarp. The fault separates hills of Tertiary strata in the hanging wall from aggrading alluvial fans in the footwall. Although the fresh scarp morphology (between arrows) indicates recent activity, the muted morphology of the hills in the hanging wall and the lack of well-developed facets in the interfluves suggest that the fault does not have a high slip rate relative to Holocene-active faults in the intermontane basins to the south. (b) View to the northeast of the contrasting vegetation and ground wetness that marks the North Kyrkungey fault (between arrows) where it crosses the floodplain of the southeastward flowing Kashkasu River. The southeast side of the fault is uplifted relative to the northwest side. (c) View to the northeast along the fault scarp (middle is marked by the red fault line) across the floodplain of the Kashkasu River. Hand-level measurements across the scarp suggest a scarp height of 1 ± 0.5 m. (d) Histogram showing probability distribution of slip rate for the North Kyrkungey fault. Minimum rate is shown with an extra significant figure to distinguish it from zero.

Figure 20. (a) View to the south of the South Kyrkungey fault. The north-vergent fault here displaces the QII(2) terrace in the hanging wall against small fans and the modern floodplain of the Bogoshti-Kakasu River, which lies west of the Kashkasu River. East of the photo the older terrace is preserved in the footwall of the fault, which is the location of the topographic profile shown in b (see also Figure 18). (b) Profile of the QII(2) terrace surface across the

south-dipping South Kyrkungey fault. Inset histogram shows the probability distribution of slip rate for the fault.

Figure 21. Map showing recently active faults and fault slip rates. Gray scale changes indicate 1500, 2500, 3500, and 4500 m contours. Vertical arrow in lower left corner represents 5 mm/yr slip rate. The arrows point in the up-dip direction and are oriented perpendicular to local fault strike, to emphasize that the data represent the dip-slip portion of fault slip only. The slip rate values and 95% confidence intervals are shown on the right. The north-south components of the shortening rates are projected along fault strike to profile line A-B. Triangles show GPS stations used to compare north-south shortening rate in Figure 22 [*Herring et al.*, ms. in prep.]. The north component of velocities at each GPS site were measured relative to station AZOK, which lies north of this map.

Figure 22. Comparison of cumulative late Quaternary geologic shortening rates and current geodetic shortening rates (relative to station AZOK) along a north-south transect through the Kyrgyz Central Tien Shan [*Herring et al.*, ms. in prep.]. Geologic shortening rates of faults that are inferred to intersect at shallow depths (e.g., Akchop Hills fault and South Kochkor fault) are combined. Dashed lines show the 95% minimum and maximum cumulative geologic shortening rate, with vertical jumps at the faults to indicate rigid blocks separating the faults. Total north velocity and the pattern of distributed shortening rate are consistent between the data sets.

Figure A1. Analysis of a faulted river terrace. The figure shows surveyed points along a terrace tread that has been cut by a fault. The dashed thin gray lines indicate the hanging wall, footwall, and scarp surfaces that are represented by linear equations of the form $y = mx + b$, in a horizontal-vertical reference frame. The thick gray line represents the fault and has a dashed projection up-dip. The scarp face and fault dip, δ, are measured positive in opposite directions. Figure A2 explains the calculations for vertical separation and dip slip.

Figure A2. Dip slip calculation for a faulted river terrace. (a) Equations for vertical separation, *v*, and dip slip, *s*, for terraces with the same hanging wall and footwall slopes. (b) Equations for vertical separation and dip slip for terraces with different hanging wall and footwall slopes. Fault dip slip, *s*, depends on the position or projection of the fault within the scarp, $P(x,y)$. *s* can be expressed as the sum of slip above point *P* (s_h) and slip below point *P* (s_f). The components of slip s_h and s_f can be calculated from the lines expressing the hanging wall ($y_h = m_h x + b_h$), footwall ($y_f = m_f x + b_f$) and scarp surface ($y_s = m_s x + b_s$), and the vertical distances from *P* to lines expressing the hanging wall ($h = h_1 + h_2$) and footwall ($f = f_1 + f_2$).

Figure B1. (a) Schematic illustration of terrace deformation predicted by fault-bend fold theory [*Suppe*, 1983]. The strath terrace is an unconformity that is displaced along with underlying layered strata that deform by slip on a fault. The diagram illustrates the case for strata oriented parallel to the underlying fault (α = δ), an assumption we make in this study for the Issyk-Ata and Akchop Hills faults (Alamedin and Djuanarik river terraces, respectively). A constant magnitude of slip, *s*, occurs along the fault surface; bedding-parallel shear within the Tertiary strata accommodates slip across the fault bend. The profile of the river terrace at its time of formation, $r(t_o)$, is indicated by the dashed line, here shown to indicate a relative rise in river level since the time of terrace formation. (b) Equation B1 shows the calculation of displacement from the change in terrace height across the fault bend and the dips of the underlying fault. Also derived is the relationship between the angle of the backlimb of the terrace, ψ, and the fault dips δ_1 and δ_2 (Equation B2). The amount of relative vertical change of the river, h_r, since the terrace was formed, is derived in Equation B3.

Figure C1. Calculation of uncertainties from measurements of slip rate variables. Column 1 indicates measurements made in the field or laboratory, and Column 2 shows the probability representations of the different variables that go into the Monte Carlo simulation. (a) Linear regression of survey points on a terrace represents a hanging wall or footwall. Solid line indicates least-squares fit and dashed curved lines represent 95% confidence ranges given standard errors in slope, m, and intercept, b. (b) Measurements or constrains on the dip, δ, and location of a fault projecting onto a scarp, x, are represented by normal, uniform, or discrete distributions. A trapezoidal distribution is shown here. Elastic strain accumulation, Δs, is represented by a uniform distribution. (c) Calibration of a radiocarbon age, showing probability density of calibrated ages. The discrete probability density of the calibrated age is represented in the error analysis if the offset unit is constrained by one radiocarbon age. Column 3 shows an example of a histogram of slip rate. The slip-rate numbers that correspond to black histogram bars are midpoints for bins, and indicate the most probable value and 95% confidence limits.

Figure C2. Age analysis of the QIII(2) terrace at the Kadjerty River, Naryn basin, using the publicly available program OxCal 3.5 [*Ramsey*, 1995]. The goal is to statistically describe the age distribution of the terrace forming "event", which is represented by the contact between coarse gravel and overlying silt and sand. (a) Radiocarbon sample ages and calibrated age distributions for three detrital charcoal samples. Overlying the "event" is the calibrated age distribution of the pooled mean radiocarbon age of two statistically similar detrital charcoal samples collected from above the gravel contact (similarity test described in *Ward and Wilson* [1979]). Calibrated ages of the individual charcoal samples are shown above by dashed lines. Underlying the "event" is the calibrated age of the charcoal sample collected below the gravel contact. (b) Age analysis of the "event" using Bayesian statistical methods described by *Ramsey* [1998]. The calibrated age distributions of the original samples above and below the event are in black lines. Grey area indicates the reweighted age distribution based on the additional constraint of stratigraphic order. The *a posteriori* age distribution of the "event" is determined from the reweighted distributions of the sample ages and an unconstrained *a priori* distribution of the "event". The agreement index indicates the extent to which the final (*a posteriori*) sample age distribution overlaps with the original (*a priori*) sample distribution. Index values below 60% are questionable (this level of disagreement is very similar to that for the 5% level chi squared test). In this example, the overall agreement index A exceeds the critical agreement $A'c$.

Figure D1. Conversion from fault dip slip to horizontal shortening. (a) Relationship between amount of horizontal shortening x_1 and slip s_2 on a shallow fault that dips at an angle δ_2. (b) North component of shortening rate $u_{n\text{-}s}$ constrained to between the pure dip slip direction and due north-south.

Table captions

Table 1. Radiocarbon ages and calibration of charcoal samples.

Table 2. TL and IRSL data and ages of QII(2) terraces.

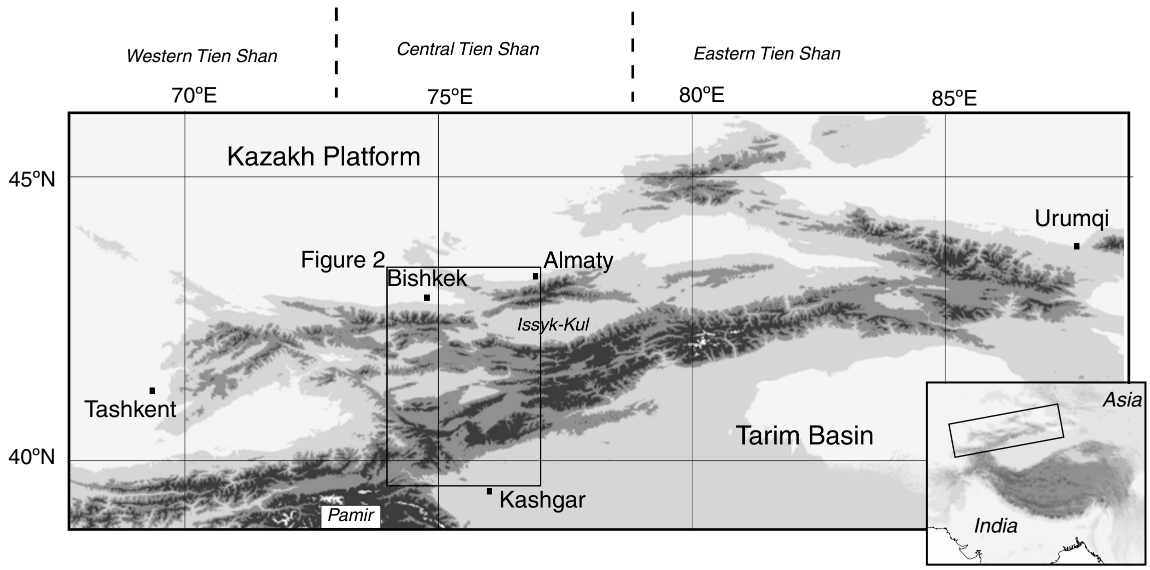

Figure 1. Map of the Tien Shan, with shades of grey indicating 1000, 2500, 3500, and 5500 m elevation contours. Approximate boundaries between the Western, Central, and Eastern Tien Shan indicated at the top of the map. Inset map shows the location of the Tien Shan in central Asia, and the box outlines the location of Figure 2.

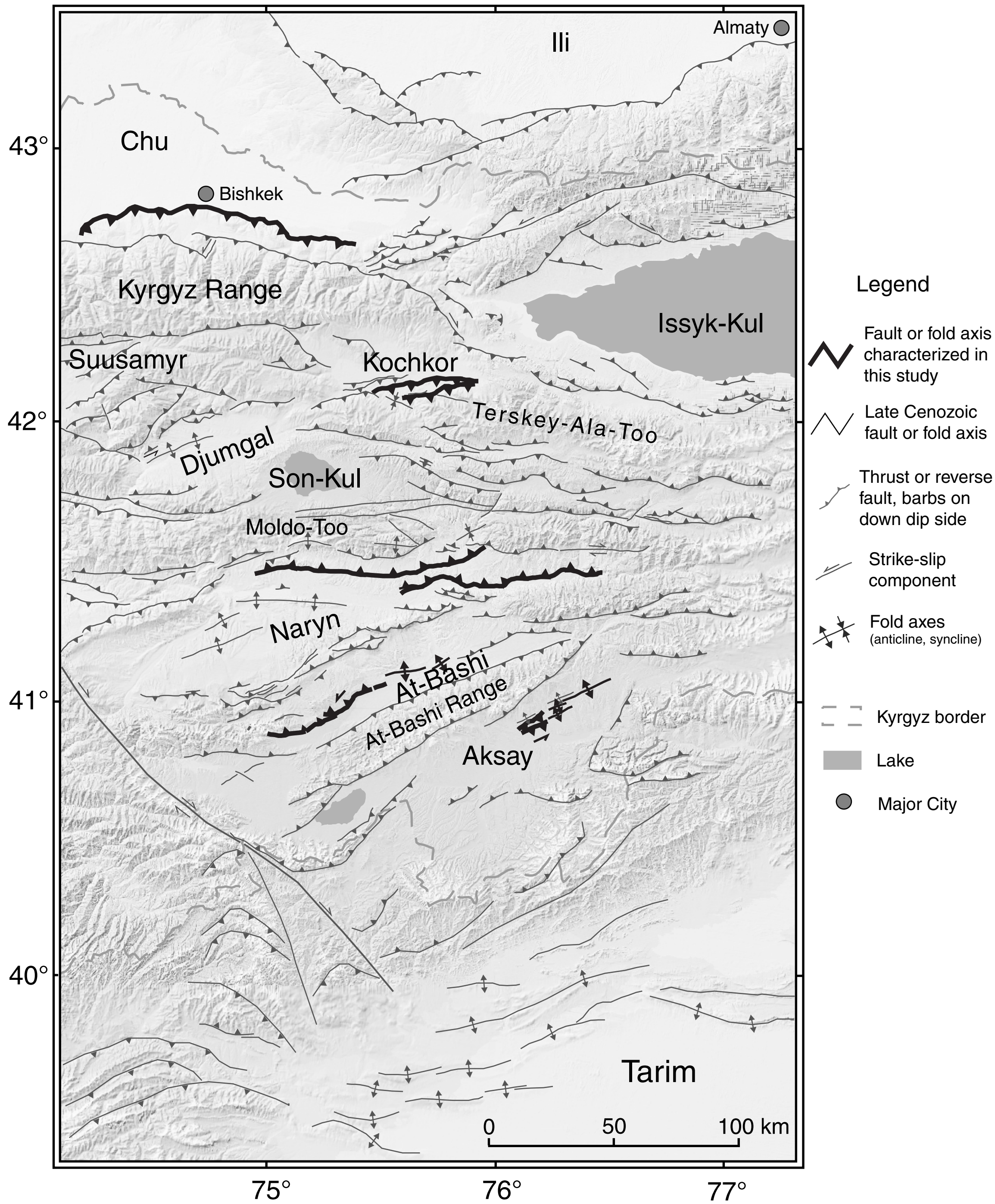

Figure 2. Preliminary map of active faults and folds in the central Tien Shan plotted with shaded relief. Major intermontane basins and lakes, and selected ranges, are labeled. Thick lines are faults and folds for which we have determined late Quaternary slip rates. The mapped fault and fold traces are from a compilation of satellite and air photo interpretation, field observations, and previous and ongoing studies.

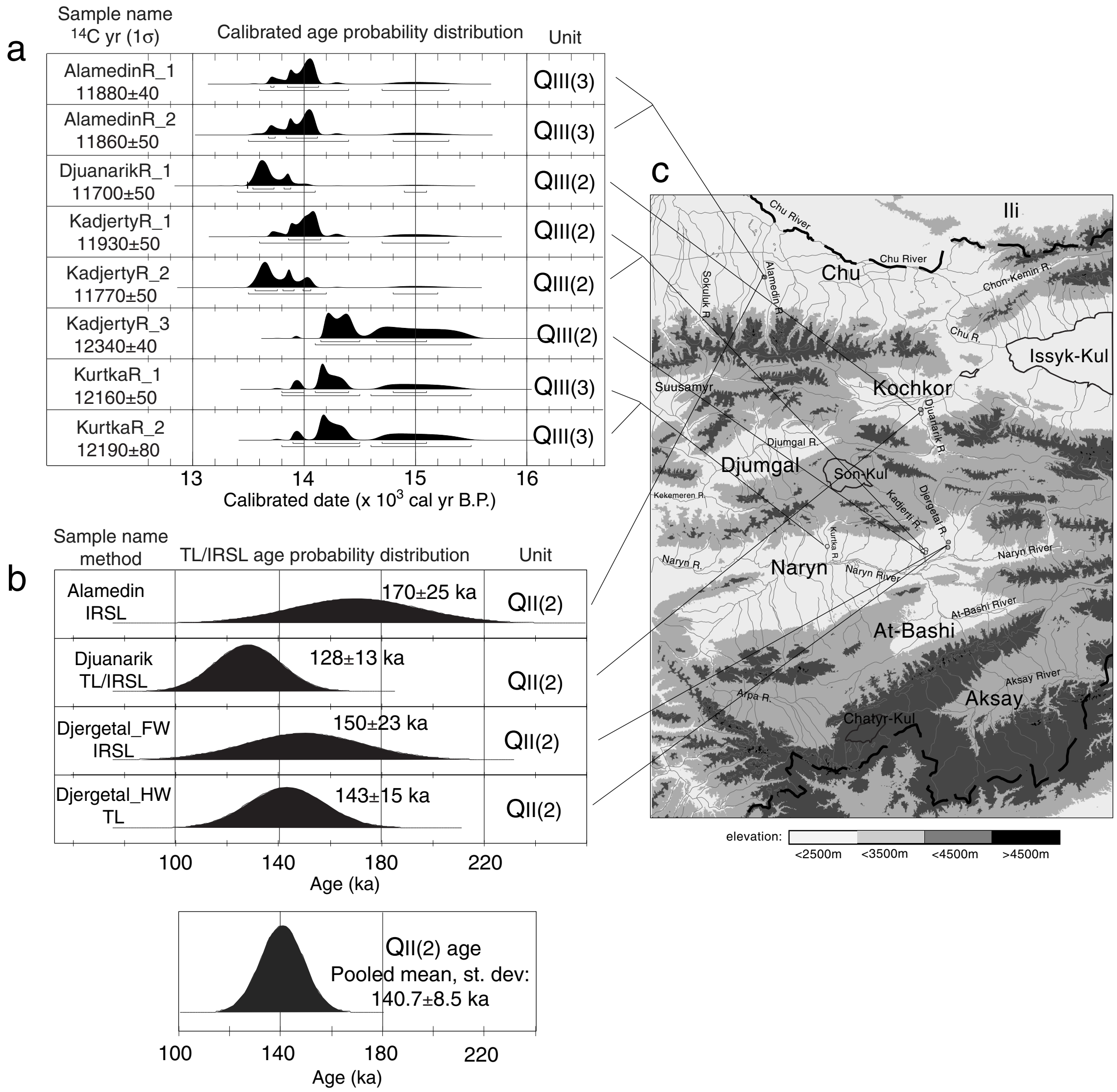

Figure 3. (a) Radiocarbon calibrated age probability distributions for 8 detrital charcoal samples collected from the QIII(2) and QIII(3) river terraces (Table 1). The similar calibrated age ranges suggest that river incision and river terrace formation occurred during a short time interval around 13.5-15.5 x 10^3 cal yr B.P. in several intermontane basins. Calibration plots generated by Oxcal v. 3.5 [*Ramsay*, 1998] based on *Stuiver et al.* [1998]; horizontal bars beneath distributions indicate 67% and 95% confidence intervals. (b) TL and IRSL age distributions (1σ shown) of silt collected from fine-grained sediments covering QII(2) terraces (Table 2). The Djergetal River samples were collected from terrace treads correlated across a fault, and are about 5 km apart. The pooled mean age and standard distribution (square root of variance) of the four ages is shown below, and we use this distribution for the age of the QII(2) terrace. (c) Map of the central Tien Shan, showing sample locations and the river network in the Kyrgyz Republic. Map extent is similar to Figure 2.

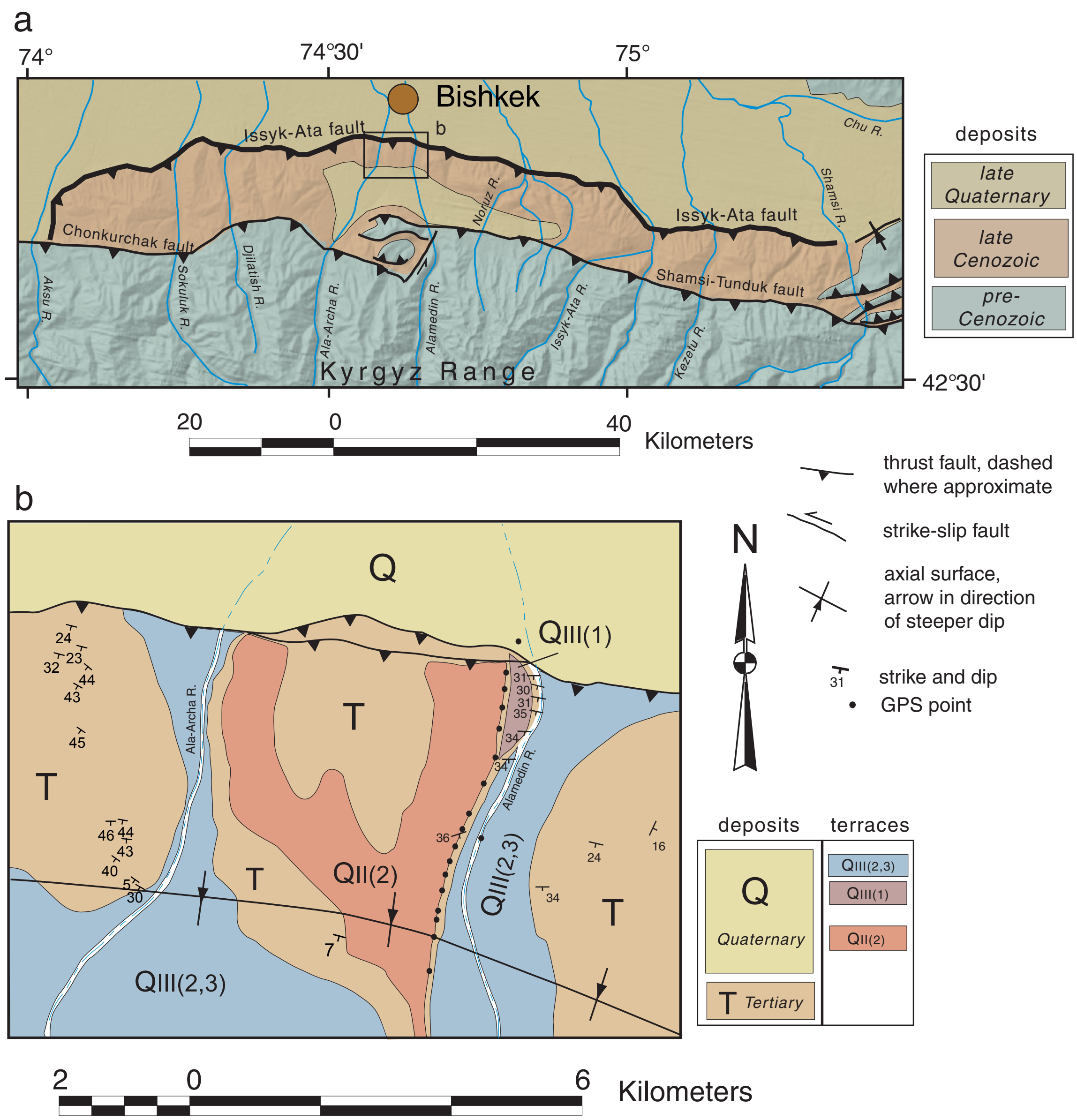

Figure 4. (a) Tectonic map of the southern Chu basin, showing major faults, geologic units, and rivers on a shaded-relief digital topographic base. (b) Geologic map of the Alamedin River site, showing terraces, differential GPS survey points, and strikes and dips of Tertiary strata.

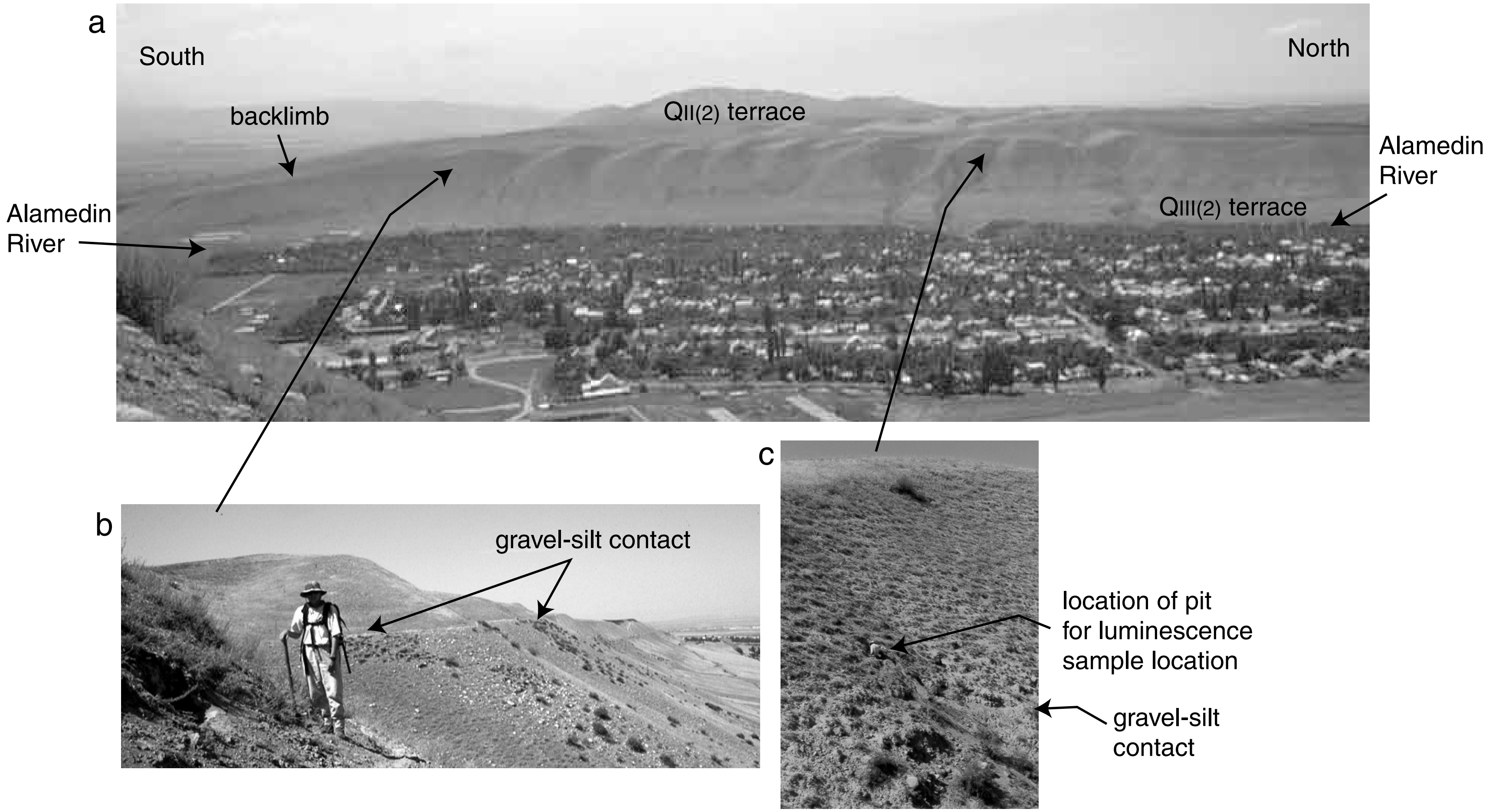

Figure 5. (a) Folded terraces of the Alamedin River (river flows to the north). Note the south-dipping QII(2) terrace surface at the south end of the photo (labeled "backlimb"), and inset QIII(2) and QIII(3) terraces (in foreground, under houses and trees). (b) View north along the contact between fluvial gravel and overlying fine-grained deposits (mostly silt) for the QII(2) terrace. (c) Pit excavated for collection of silt for luminescence dating, located ~2.5 m above the contact with fluvial gravel.

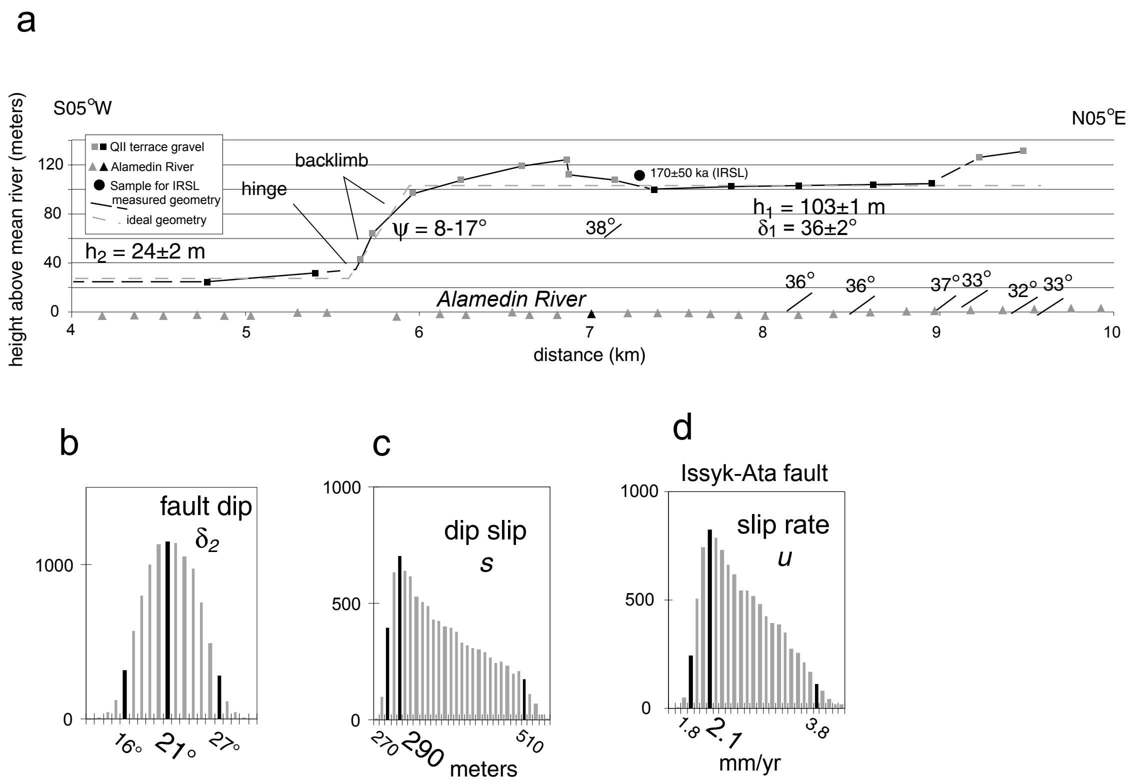

Figure 6. (a) Alamedin River profile, showing the deformed QII(2) terrace west of the river, the location and age of the sample collected for luminescence dating, and the apparent dips of Neogene strata exposed below the terraces. Points along the QII(2) terrace are from differential GPS surveying. Points along the Alamedin River are from 1:25,000-scale topographic maps with a 5-m contour interval (gray) and differential GPS (black). We remove the modern river gradient by rotating the data about a horizontal axis so that the x-axis is parallel to the gradient of the river. Apparent dips of strata are similarly rotated. Solid black lines connect surveyed points with continuous exposure; black dashed line indicates our interpretation of a hinge and secondary folding near the top of the hinge and at the northern front. The dashed gray line schematically illustrates the simplification of the geometry of the terrace; this line is constrained by the black points that define the terrace south and north of the fault bend. We base the slip-rate calculation on this simplified geometry with the values of h_1, h_2, ψ, and δ_1 indicated on the figure. The method for calculating slip rate is described in Appendix B. (b) Histogram showing the predicted value of δ_2, based on equation B2 in Appendix B. The black bars indicate the 95% confidence minimum and maximum, and the most probable value. (c) Histogram showing the predicted amount of dip slip on the Issyk-Ata fault since formation of the QII(2) terrace. (d) Histogram showing the probability distribution of slip rate.

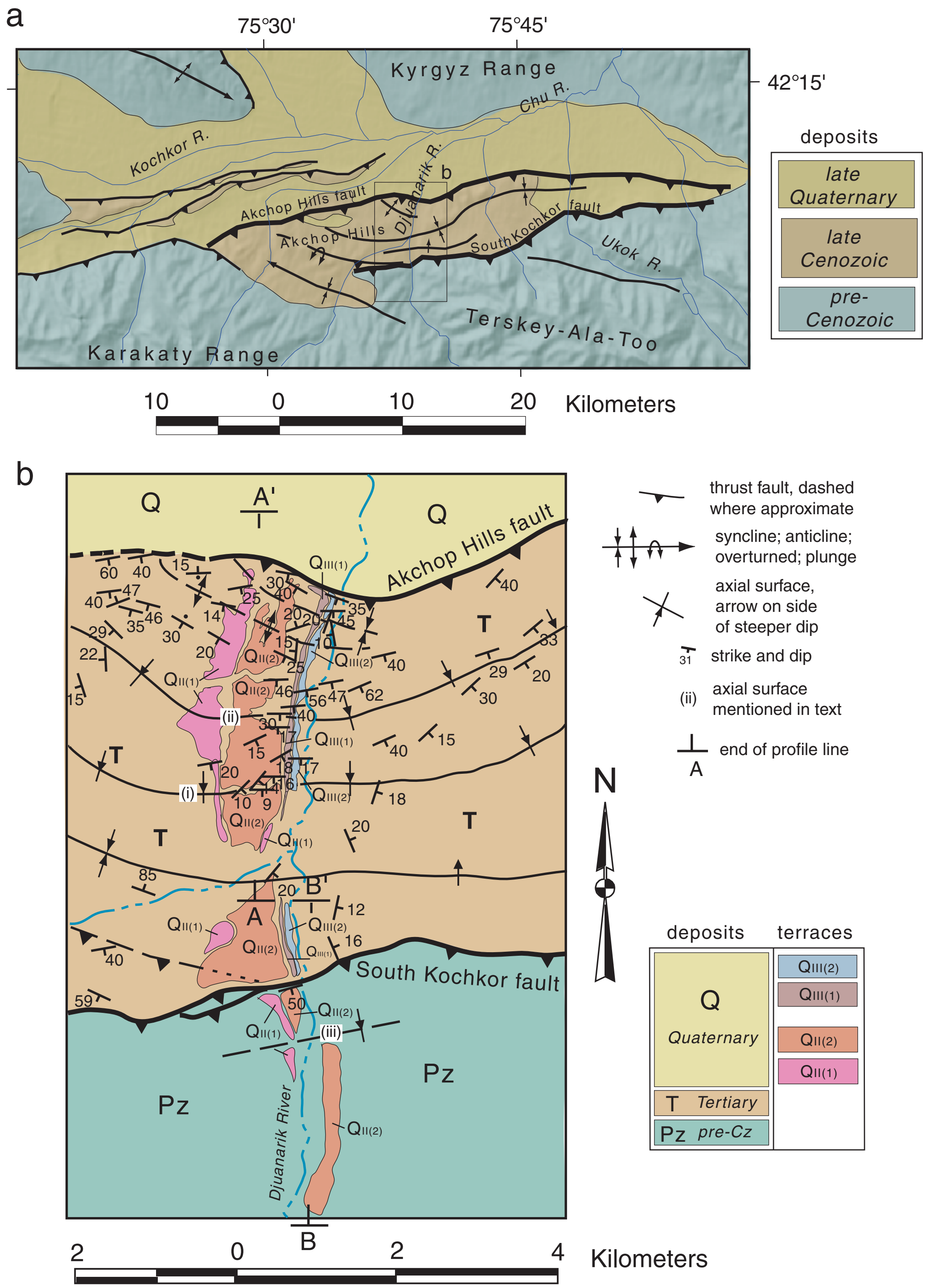

Figure 7. (a) Simplified geologic map of the southern Kochkor basin. The Akchop Hills consist of folded Tertiary strata in the hanging wall of the Akchop Hills fault. (b) Geologic map of the Djuanarik River area, showing nested terraces along the west bank of the Djuanarik River and strikes and dips of underlying strata. Axial surfaces labeled (i), (ii), and (iii) are discussed in the text and in later figures. Surveyed points along the extensive QII(2) terrace constrain our analyses of slip rate for the Akchop Hills fault (profile line A-A') and South Kochkor fault (profile line B-B').

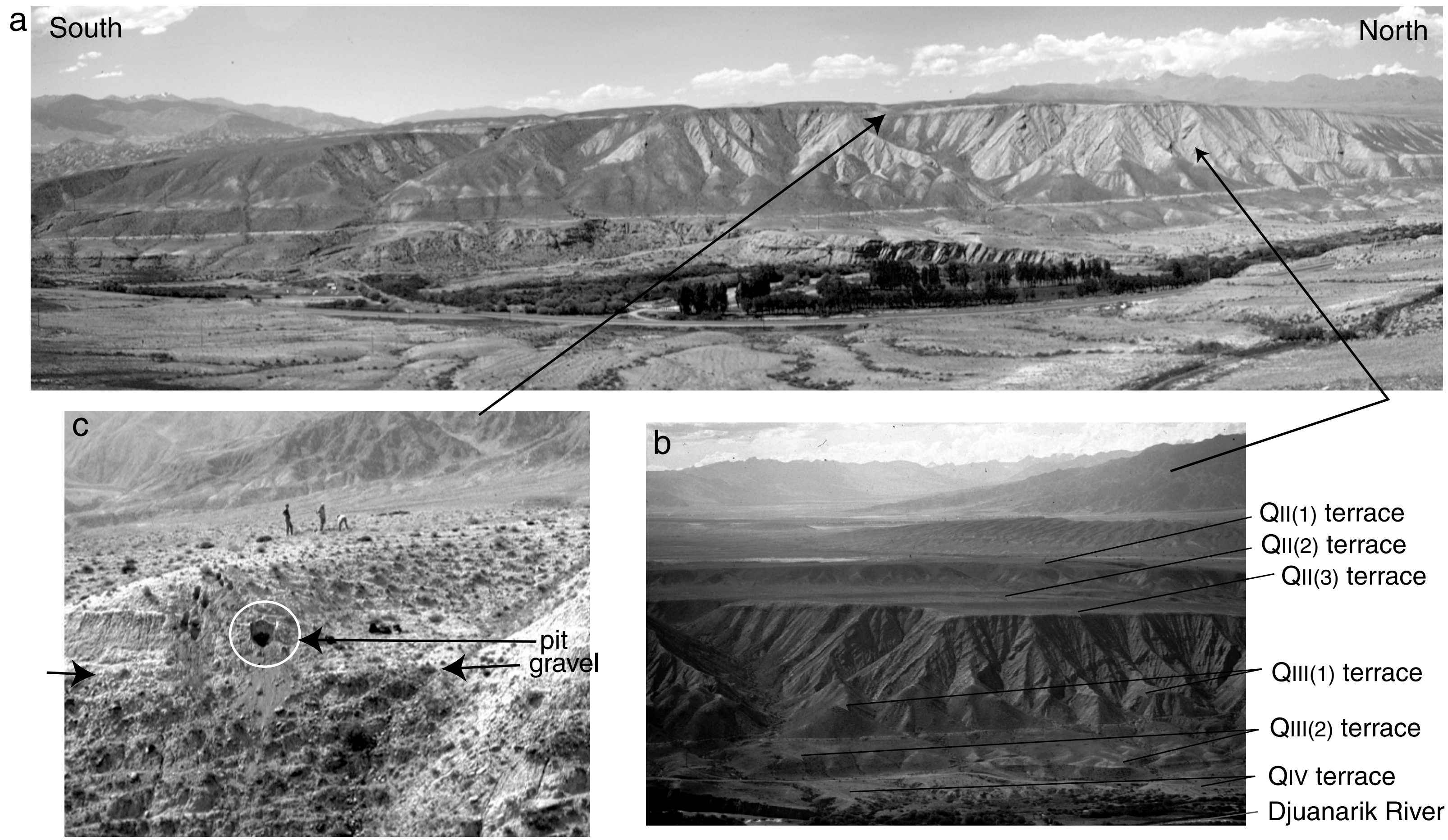

Figure 8. Nested terraces along the west side of the Djuanarik River, Kochkor basin. (a) West view of terraces and Djuanarik River (the river flows north). Arrows indicate locations of Figures b and c. (b) Northwest view of strath terraces; surfaces are labeled. Notice exposed Djuanarik Formation sandstone layers that are folded (Photo by Martin Miller). (c) South view of pit excavated for the collection of silt for luminescence dating on the QII(2) terrace (marked a with white circle). Short arrows mark the contact between fluvial gravel and overlying fine-grained sediments.

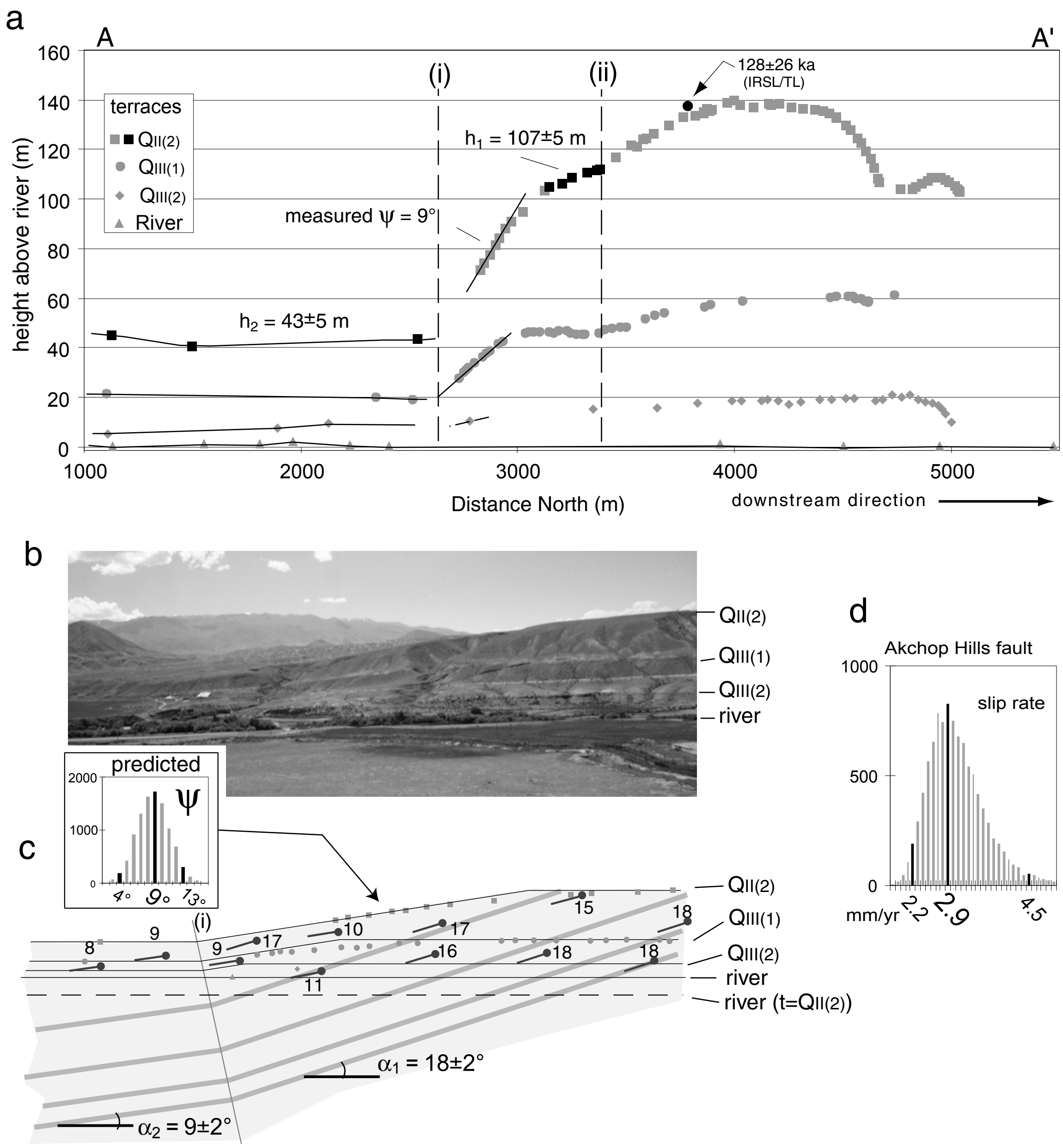

Figure 9. (a) Vertically exaggerated river terrace profiles along the Djuanarik River. Profiles were rotated counter clock-wise 0.7° so the horizontal axis would parallel the modern river. Note the progressive limb rotation and kink-band migration recorded by the backlimbs of the QIII(1) and QII(2) terraces off of active axial surfaces (i) and (ii); we infer a back limb for the QIII(2) terrace but did not sample enough points to measure it. The black squares on the QII(2) terrace were used to define the heights of the terrace across axial surface (i). (b) Photo of the backlimb of the Akchop Hills anticline across axial surface (i), showing the QII(2), QIII(1), and QIII(2) terraces. (c) Cross-section across axial surface (i), showing apparent dips of Pliocene Djuanarik Fm. strata and surveyed points along the terraces and modern river. Thick gray lines schematically illustrate dipping strata across the fold. Thin black lines show the predicted terrace profiles assuming that the terraces are deformed by ideal fault-related folding (see Appendix B). Inset box shows the predicted backlimb angle (Equation B2 in Appendix B). Horizontal dashed line shows inferred position of the river at the time of QII(2) terrace formation. (d) Histogram showing slip-rate probability distribution for the Akchop Hills fault based on Equation B1 in Appendix B.

a

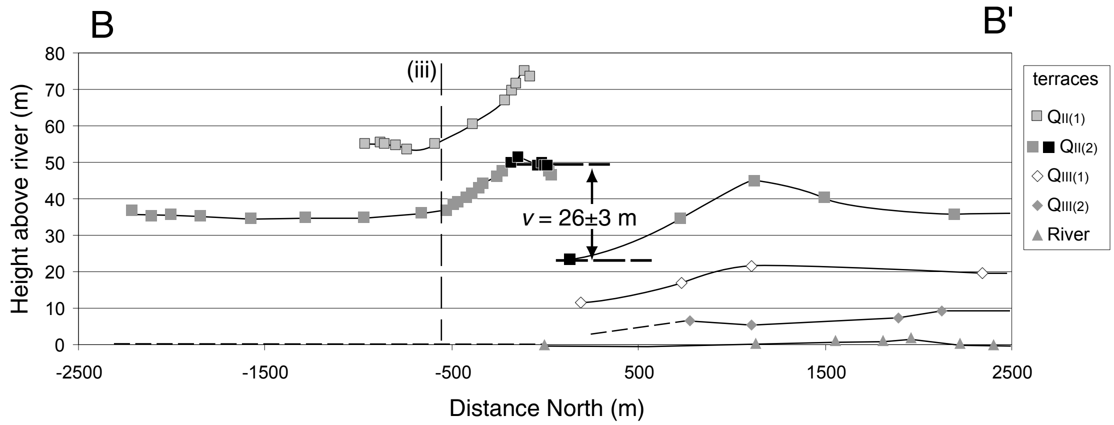

b

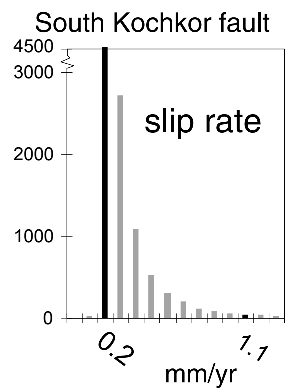

Figure 10. (a) Profile of river terraces across the South Kochkor fault, showing terrace correlation, and folding of the terraces in the hanging wall across axial surface (iii). Black points and horizontal dashed lines indicate the vertical separation used in the slip rate calculation. (b) Histogram showing slip rate calculation for the South Kochkor fault. The 0.2 mm/yr bin contains the minimum slip rate (2.5% tail). Adding another significant digit to the histogram bins yields a 0.17 mm/yr minimum slip rate.

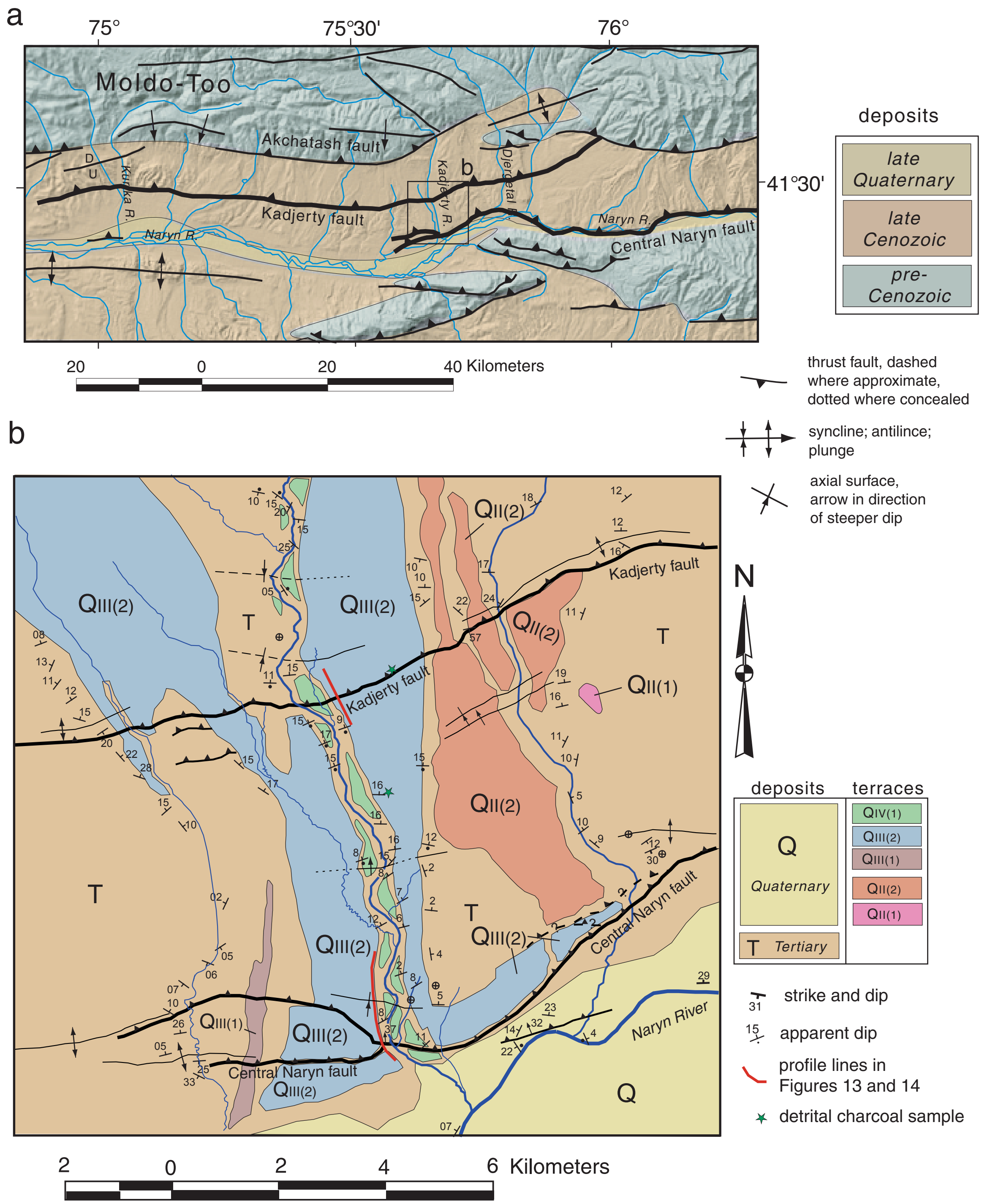

Figure 11. (a) Simplified geologic map of northeastern Naryn basin. The Kadjerty and Central Naryn fault appear to accommodate most of the shortening at the surface across the northern Naryn basin margin. We have evaluated the slip rates of the Kadjerty and Central Naryn faults along the Kadjerty River (box shows area of Figure 11b). (b) Geologic map along the Kadjerty River, showing dips of Tertiary strata, fault and fold traces, and river terraces.

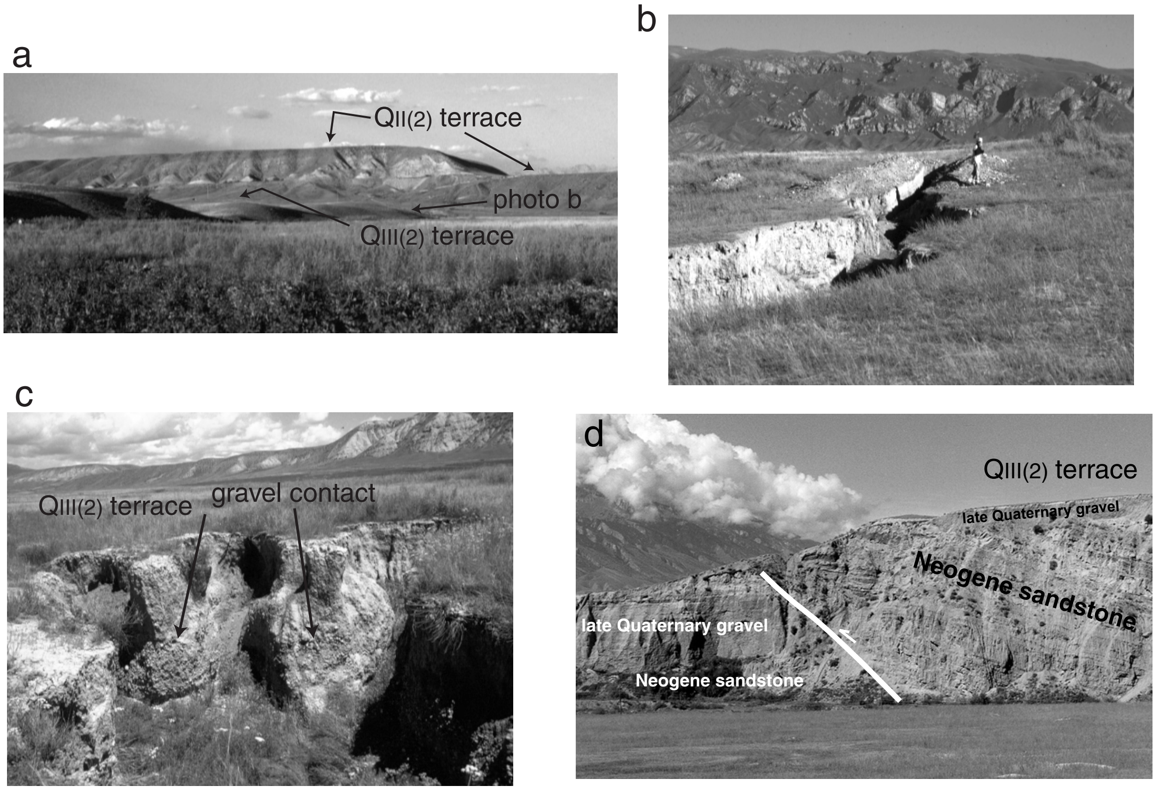

Figure 12. (a) Kadjerty fault scarp cutting nested terraces. Photo is to NE along the scarp. The fault scarp across the QII(2) terrace (in the distance) has a vertical separation of about 60 m; the fault scarp across the QIII(2) terrace to the left has a vertical separation of about 10 m. (b) Gully and trench across the QIII(2) fault scarp near the QII(2) terrace riser exposes terrace gravel and charcoal. Detrital charcoal from the top of the fluvial gravel dates to 14.1-15.4 x 10^3 cal yr B.P. (c) A gully in the QIII(2) terrace between the Kadjerty and Central Naryn faults exposes fluvial gravel and overlying fine-grained sediments. Two detrital charcoal fragments collected above the gravel contact in this exposure date to 13.5-14.1 x 10^3 cal yr B.P. Photo is to the north. (d) Central Naryn fault exposure along the Kadjerty River. View is to the southwest. The exposed fault dips 37 ± 2°N. Neogene strata in the hanging wall dip ~11-15°N. The Kadjerty River flows south along the base of the exposure. Notice thicker accumulation of late Quaternary gravel in the footwall of the fault.

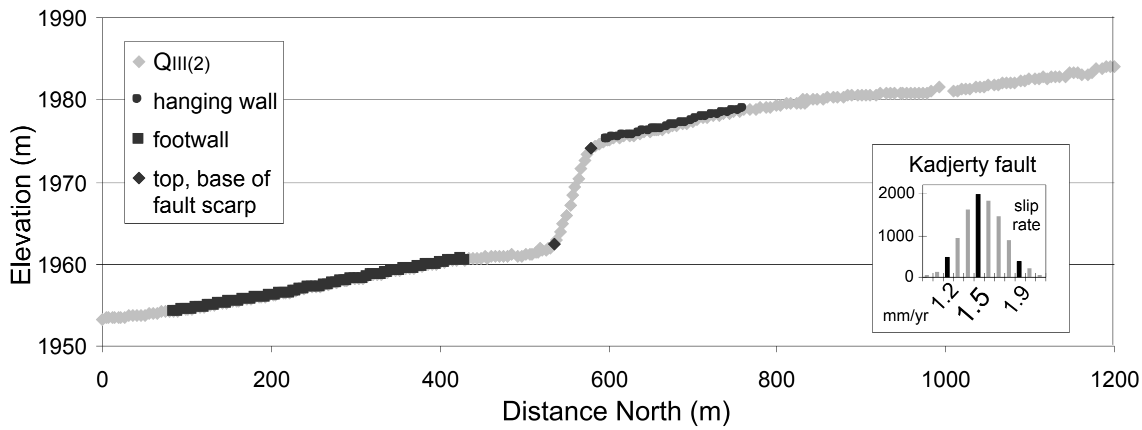

Figure 13. Profile of the QIII(2) terrace across the Kadjerty fault east of the Kadjerty River; location on Figure 11b. Black circles, squares, and diamonds indicate the points used to define the surfaces on the hanging wall, footwall, and scarp face, respectively. Inset histogram shows the slip rate distribution; the most probable slip rate and the 95% confidence minimum and maximum rates are indicated by the black bars and corresponding values.

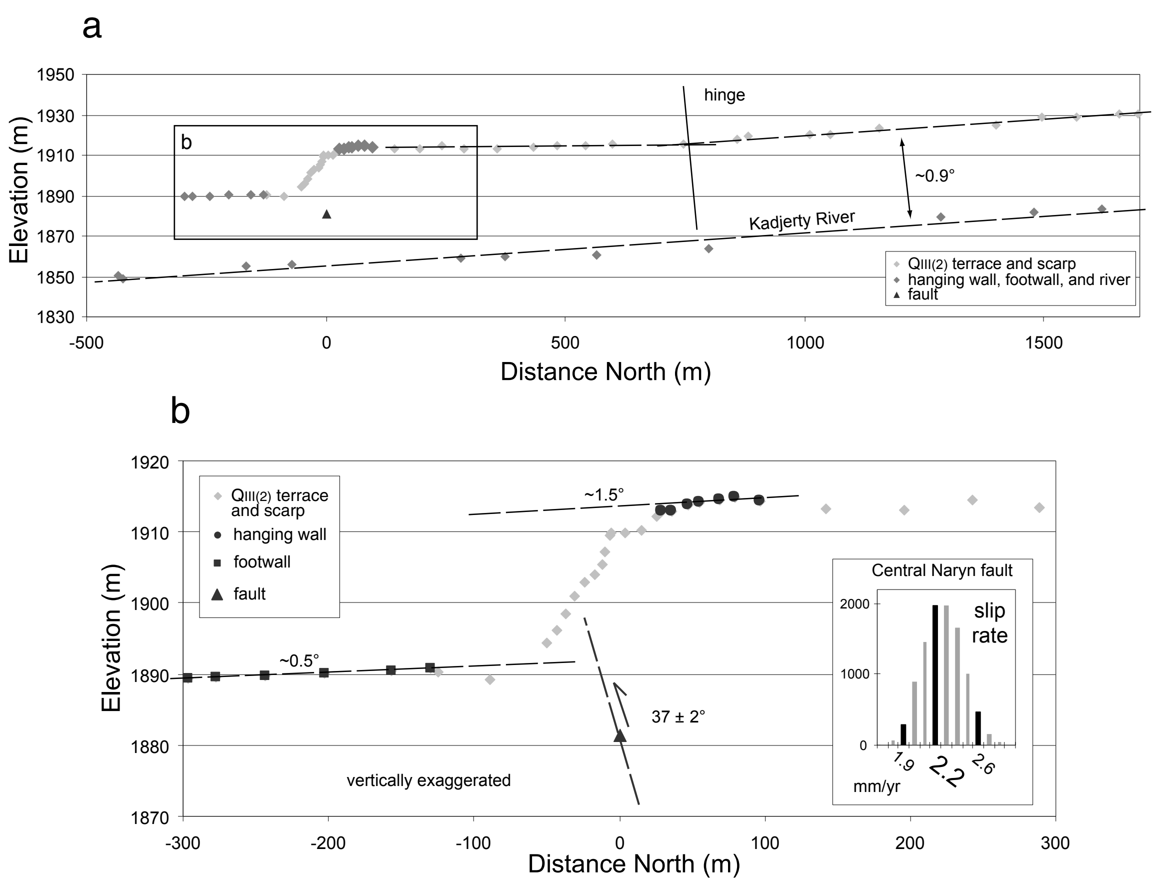

Figure 14. (a) Profile of the upper gravel contact of the QIII(2) terrace across the Central Naryn fault near the Kadjerty River; location shown on Figure 11b. The gradient of the QIII(2) terrace and the modern river are similar north of the labeled "hinge," but south of the hinge the terrace surface is subhorizontal, indicating that it has been rotated due to slip on the Central Naryn fault. (b) Close-up view of the profile across the fault scarp, showing the surveyed points used to define the hanging wall and footwall and the dips of those surfaces. A single point surveyed on the exposed fault surface and the measured dip are used to constrain the fault location in the slip rate calculation. The inset box shows the probability distribution of slip rate from the analysis. Black bars and numbers indicate the 95% confidence limits and the most probable slip rate value.

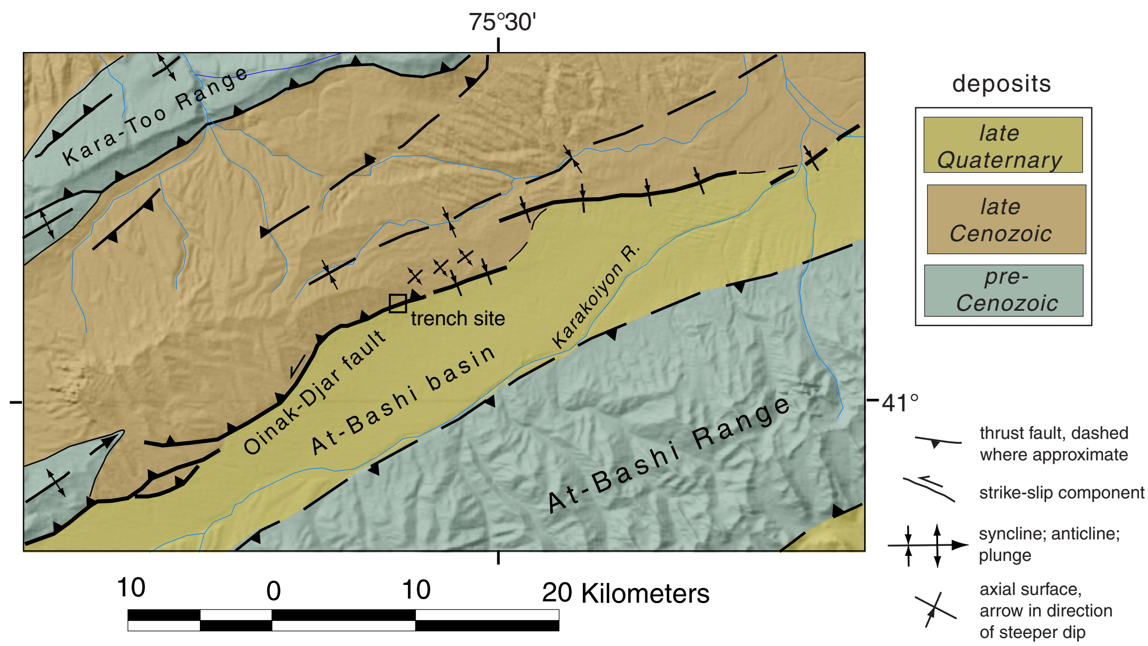

Figure 15. Simplified geologic map of the western At-Bashi basin. The Oinak-Djar fault marks the boundary between Tertiary strata and late Quaternary deposits, and defines the southeast margin of deformation for the larger structure that separates the Naryn and At-Bashi basins. The Oinak-Djar fault reaches the surface along the western half of the mapped trace; to the east the fault is blind, and the surface expression is a fault-propagation fold with a sharp synclinal axial surface. A trench excavated across the fault (boxed area) provides data to measure slip rate.

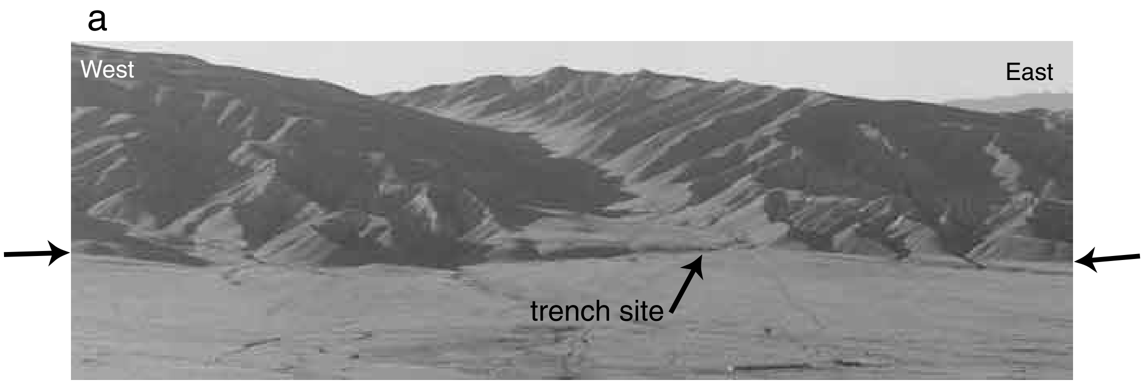

Figure 16. (a) View to the north of the Oinak-Djar fault scarp. The fault (between horizontal arrows) separates the hills of steeply dipping Tertiary strata in the hanging wall from the aggrading alluvial fans in the footwall. The trench site is situated in the eastern part of a wide wash in which multiple terrace levels are progressively displaced by recent slip on the fault. (b) View to the west along the Oinak-Djar fault scarp. The trench and spoil pile are in the foreground. The spoil pile is about 2 m high. The mounds on the fan surface in the middle left of the photo are cultural sites of uncertain age or purpose.

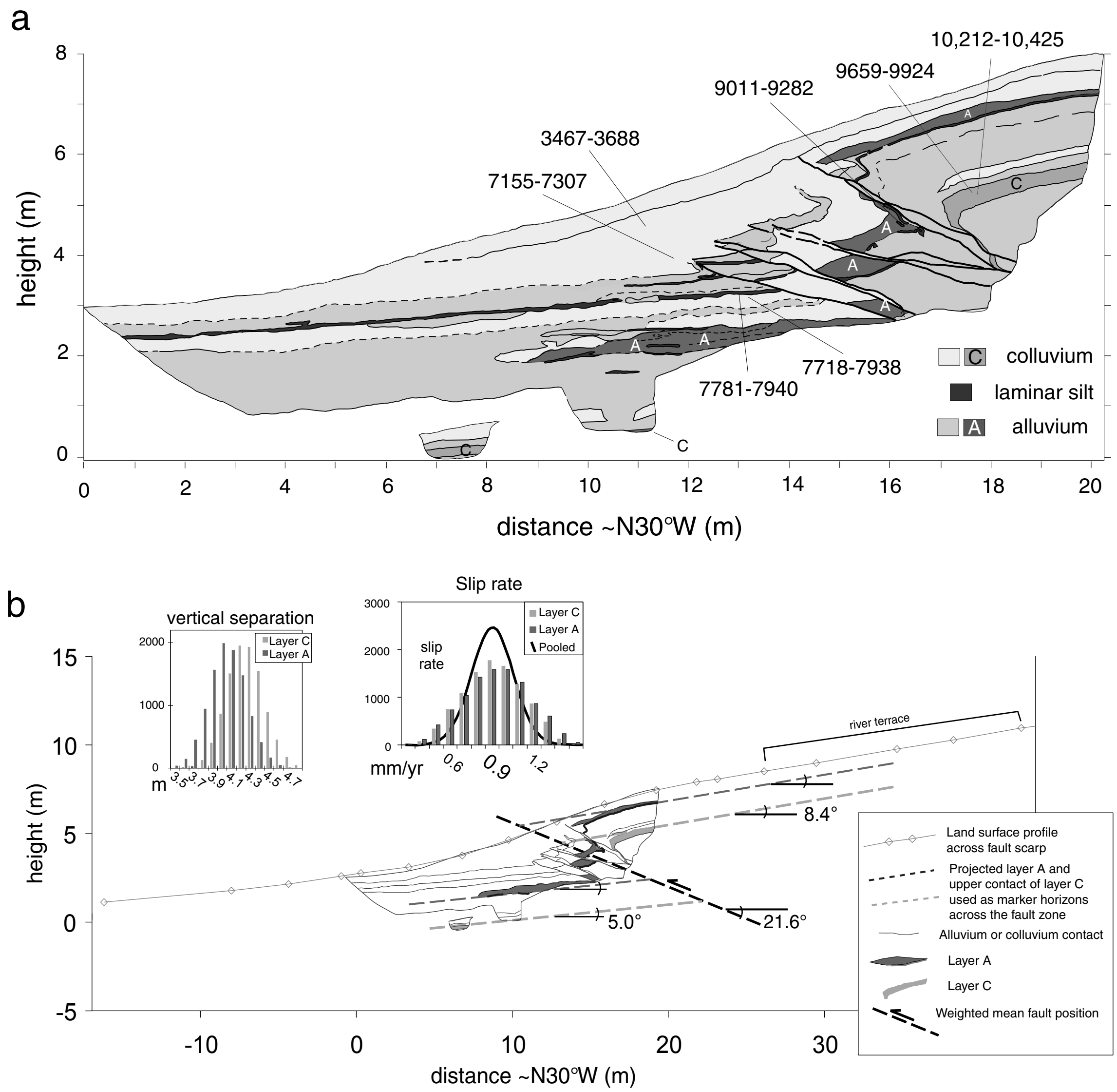

Figure 17. (a) Map of the west wall of the trench across the Oinak-Djar fault. Ages of charcoal samples are in calibrated years before present, and represent ~95% confidence limits (Table 1). We correlate layers A and C across the fault zone and use them to calculate slip rate. (b) Profile of the land surface across the trench. To calculate slip rate, we project layers A and C into the fault zone. The slopes of the projected layers in the hanging wall are based on the dip of the terrace surface north of the trench. Changes in layer dip near the fault are interpreted to be due to drag folding. Histograms show the similar amounts of vertical separation and slip rate. The line in the slip rate histogram shows the pooled mean slip rate and uncertainty by combining the two measurements.

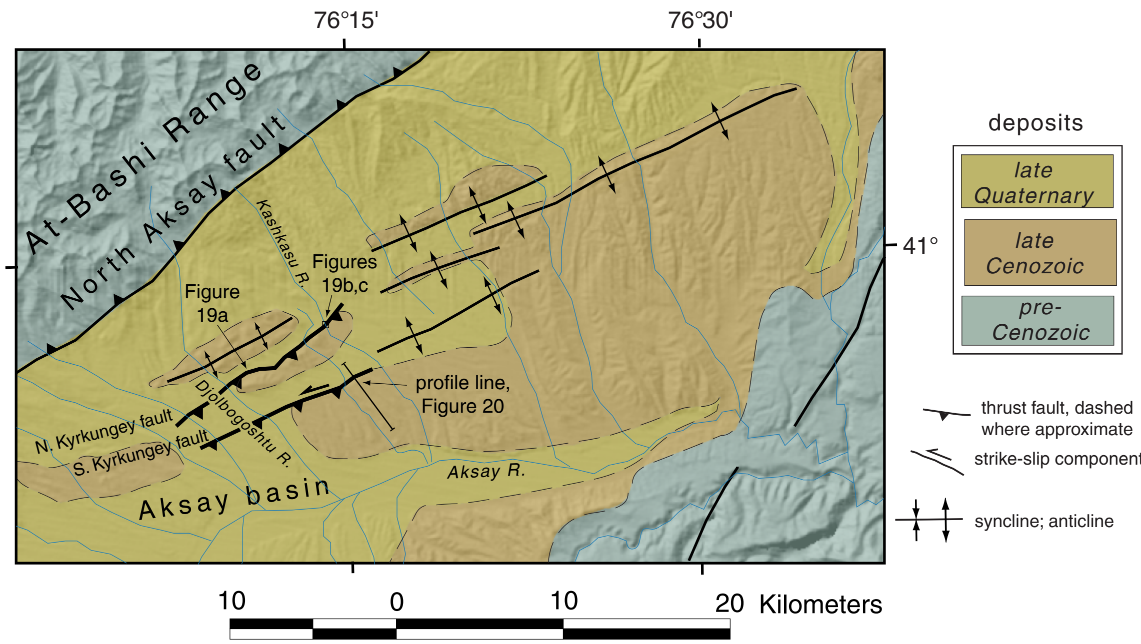

Figure 18. Simplified geologic map of the eastern Aksay basin. The North and South Kyrkungey faults are part of a zone of late Quaternary folds within the northeastern Aksay basin, and appear to accommodate most of the shortening across the basin. Late Quaternary deposits include large amounts of glacial till and outwash; large moraines from the last glacial period are preserved along the southern At-Bashi Range front and are not offset by more than ~1 m by the North Aksay fault. Locations of photos in Figure 19 and profile line in Figure 20 are shown.

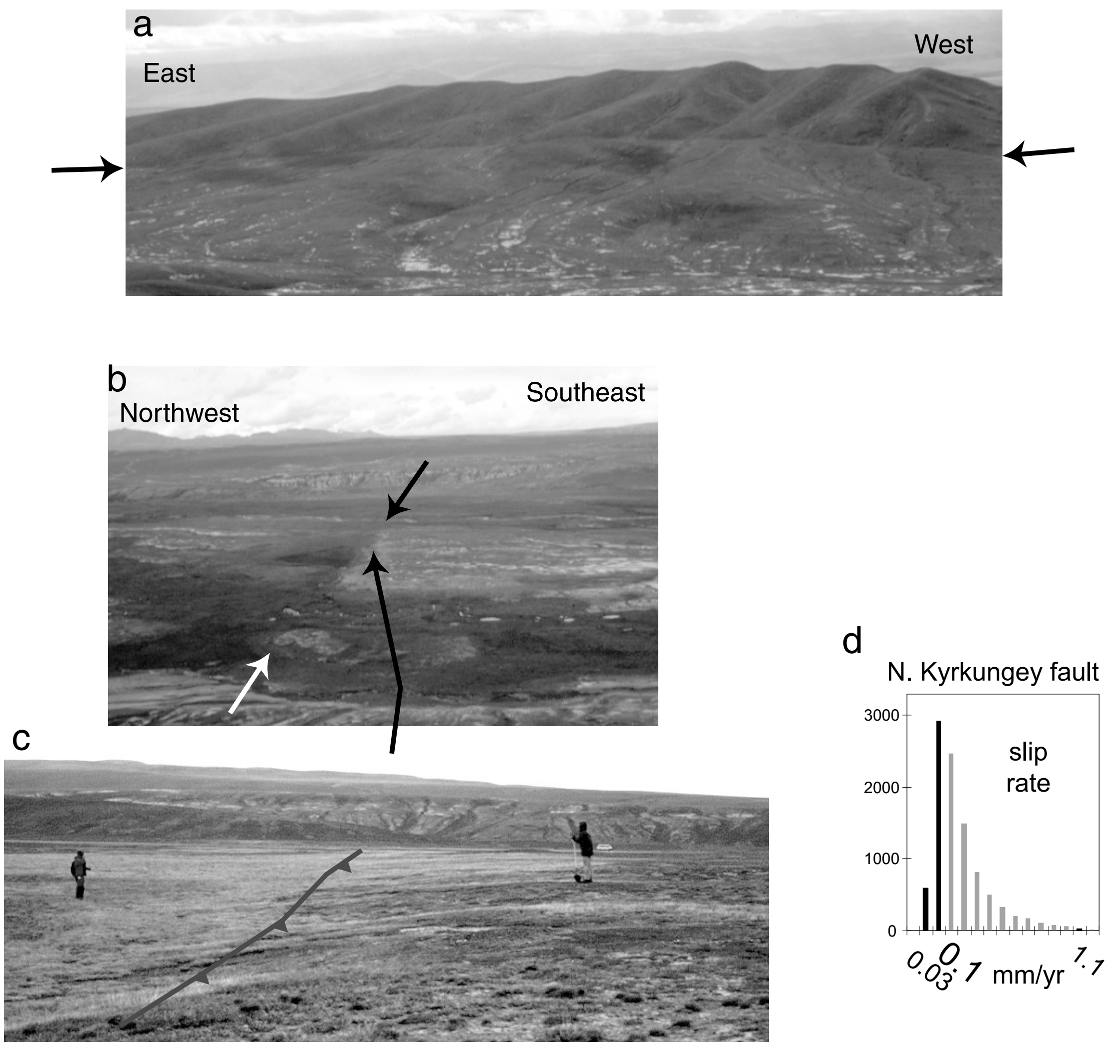

Figure 19. (a) View to the south of the North Kyrkungey fault scarp. The fault separates hills of Tertiary strata in the hanging wall from aggrading alluvial fans in the footwall. Although the fresh scarp morphology (between arrows) indicates recent activity, the muted morphology of the hills in the hanging wall and the lack of well-developed facets in the interfluves suggest that the fault does not have a high slip rate relative to Holocene-active faults in the intermontane basins to the south. (b) View to the northeast of the contrasting vegetation and ground wetness that marks the North Kyrkungey fault (between arrows) where it crosses the floodplain of the southeastward flowing Kashkasu River. The southeast side of the fault is uplifted relative to the northwest side. (c) View to the northeast along the fault scarp (marked by the fault line) across the floodplain of the Kashkasu River. Hand-level measurements across the scarp suggest a height of 1 ± 0.5 m. (d) Histogram showing probability distribution of slip rate for the North Kyrkungey fault. Minimum rate is shown with an extra significant figure to distinguish it from zero.

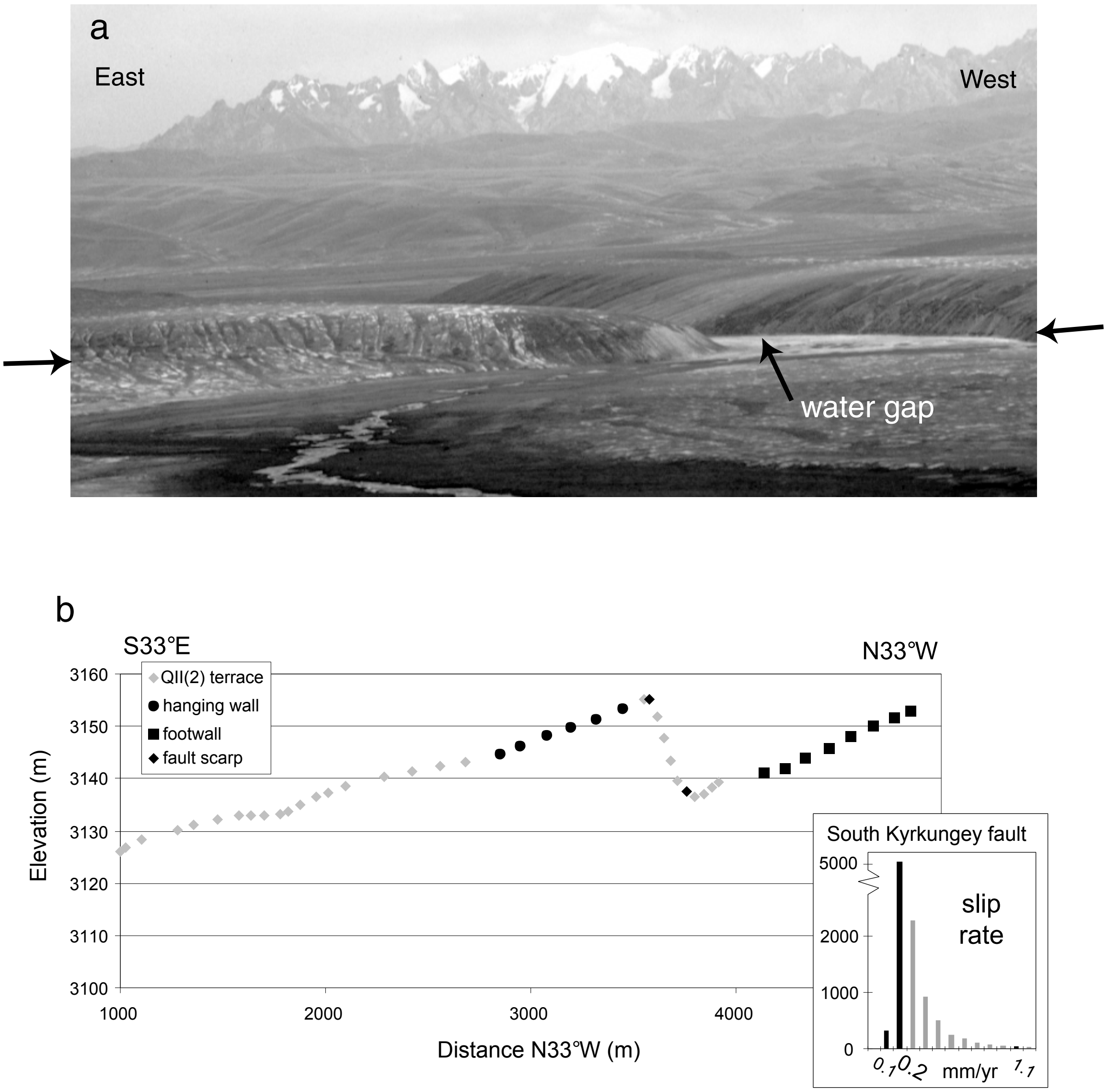

Figure 20. (a) View to the south of the South Kyrkungey fault. The north-vergent fault here displaces the QII(2) terrace in the hanging wall against small fans and the modern floodplain of the Bogoshti-Kakasu River, which lies west of the Kashkasu River. East of the photo the older terrace is preserved in the footwall of the fault, which is the location of the topographic profile shown in b (see also Figure 18). (b) Profile of the QII(2) terrace surface across the south-dipping South Kyrkungey fault. Inset histogram shows the probability distribution of slip rate for the fault.

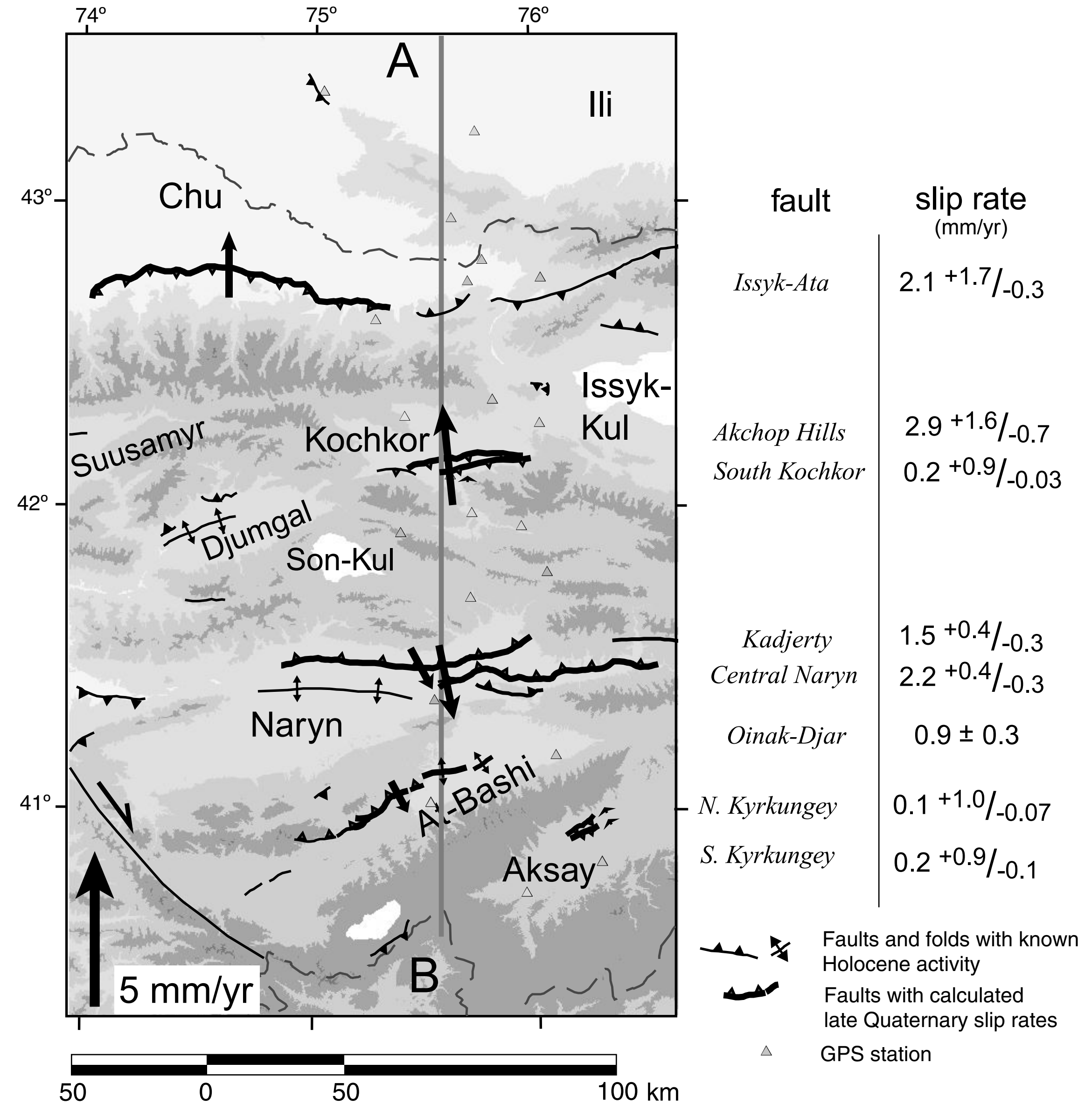

Figure 21. Map showing recently active faults and fault slip rates. Gray scale changes indicate 1500 m, 2500, 3500, and 4500 m contours. Vertical arrow in lower left corner represents 5 mm/yr slip rate. The arrows point in the up-dip direction and are oriented perpendicular to local fault strike, to emphasize that the data represent the dip-slip portion of fault slip only. The slip rate values and 95% confidence intervals are shown on the right. The north-south components of the shortening rates are projected along fault strike to profile line A-B. Triangles show GPS stations used to compare north-south shortening rate in Figure 22 [*Herring et al.*, ms. in prep.]. The north component of velocities at each GPS site were measured relative to station AZOK, which lies north of this map.

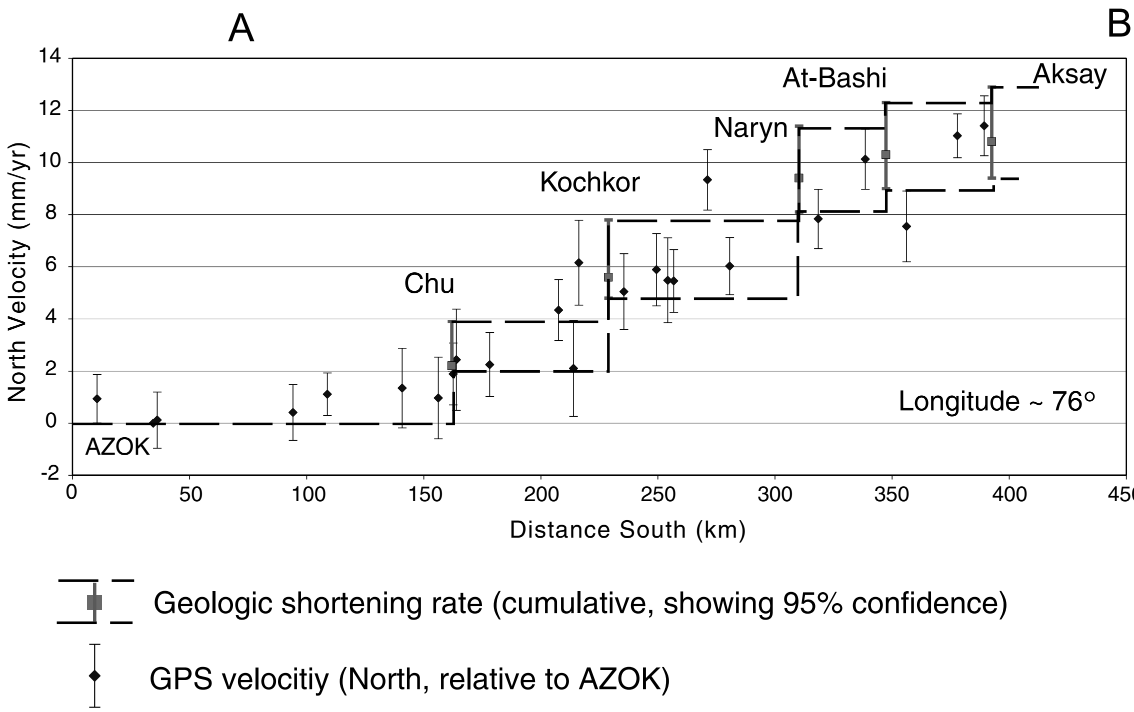

Figure 22. Comparison of cumulative late Quaternary geologic shortening rates and current geodetic shortening rates (relative to station AZOK) along a north-south transect through the Kyrgyz Central Tien Shan [*Herring et al.*, ms. in prep.]. Geologic shortening rates of faults that are inferred to intersect at shallow depths (e.g., Akchop Hills fault and South Kochkor fault) are combined. Dashed lines show the 95% minimum and maximum cumulative geologic shortening rate, with vertical jumps at the faults to indicate rigid blocks separating the faults. Total north velocity and the pattern of distributed shortening rate are consistent between the data sets.

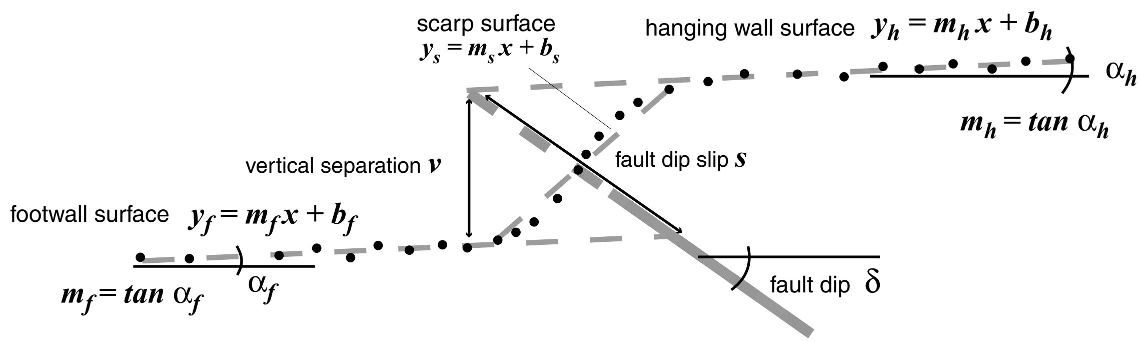

Figure A1. Analysis of a faulted river terrace. The figure shows surveyed points along a terrace tread that has been cut by a fault. The dashed thin gray lines indicate the hanging wall, footwall, and scarp surfaces that are represented by linear equations of the form y = mx+b, in a horizontal-vertical reference frame. The thick gray line represents the fault and has a dashed projection up-dip. The scarp face and fault dip, δ, are measured positive in opposite directions. Figure A2 explains the calculations for vertical separation and dip slip.

a

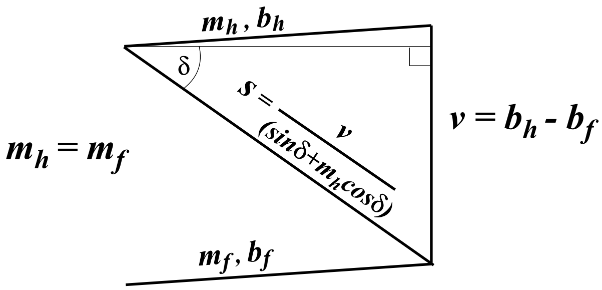

b

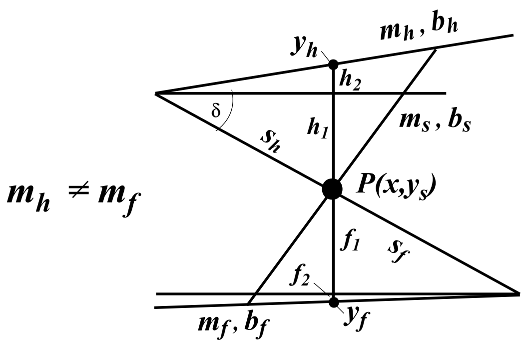

$$v(x) = y_h - y_f = m_h x + b_h - m_f x + b_f$$
$$= x(m_h - m_f) + b_h - b_f$$

$$h = h_1 + h_2 = y_h - y_s$$
$$= x(m_h - m_s) + b_h - b_s$$

$$f = f_1 + f_2 = y_s - y_f$$
$$= x(m_s - m_f) + b_s - b_f$$

$$h_1 = s_h \sin\delta$$
$$h_2 = s_h m_h \cos\delta$$

$$f_1 = s_f \sin\delta$$
$$f_2 = s_f m_f \cos\delta$$

$$x(m_h - m_s) + b_h - b_s$$
$$= s_h \sin\delta + s_h m_h \cos\delta$$

$$x(m_s - m_f) + b_s - b_f$$
$$= s_f \sin\delta + s_f m_f \cos\delta$$

$$s_h = \frac{x(m_h - m_s) + b_h - b_s}{\sin\delta + m_h \cos\delta} \qquad s_f = \frac{x(m_s - m_f) + b_s - b_f}{\sin\delta + m_f \cos\delta}$$

$$s = s_h + s_f$$

Figure A2. Dip slip calculation for a faulted river terrace. (a) Equations for vertical separation, *v*, and dip slip, *s*, for terraces with the same hanging wall and footwall slopes. (b) Equations for vertical separation and dip slip for terraces with different hanging wall and footwall slopes. Fault dip slip, s, depends on the position or projection of the fault within the scarp, P(x,y). s can be expressed as the sum of slip above point P (s_h) and slip below point P (s_f). The components of slip s_h and s_f can be calculated from the lines expressing the hanging wall ($y_h = m_h x + b_h$), footwall ($y_f = m_f x + b_f$) and scarp surface ($y_s = m_s x + b_s$), and the vertical distances from P to lines expressing the hanging wall ($h = h_1 + h_2$) and footwall ($f = f_1 + f_2$).

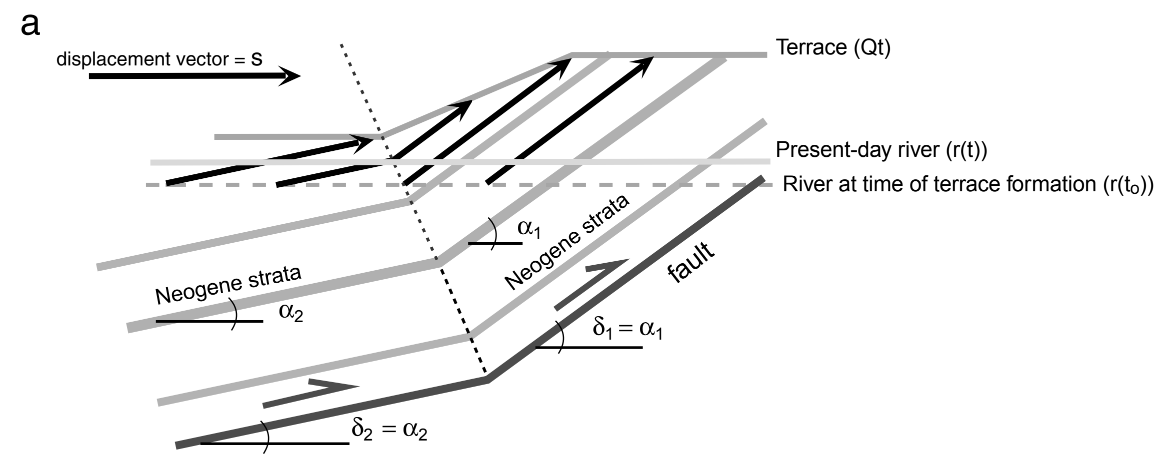

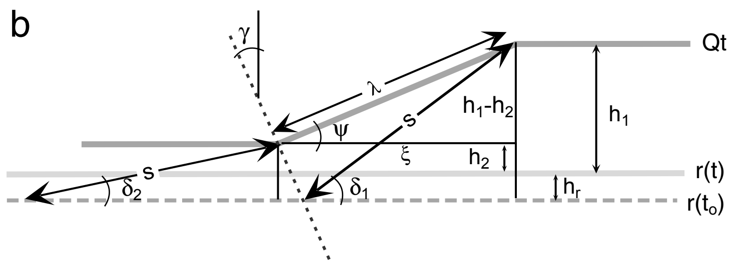

$$s = \frac{(h_1+h_r)}{\sin \delta_1} = \frac{(h_2+h_r)}{\sin \delta_2}$$

$$s = \frac{h_1-h_2}{\sin \delta_1 - \sin \delta_2} \qquad \text{(B1)}$$

$$\psi = \arctan\left[(h_1-h_2)/\xi\right]$$

$$h_1-h_2 = s(\sin \delta_1 - \sin \delta_2)$$

$$\xi = s \cos \delta_1 + (h_2+h_r) \tan \gamma;$$

$$h_2+h_r = s \sin \delta_2$$

$$\gamma = (\alpha_1 + \alpha_2)/2$$

$$\psi = \arctan\left[\frac{\sin \delta_1 - \sin \delta_2}{\cos \delta_1 + \sin \delta_2 \tan ((\alpha_1 + \alpha_2)/2)}\right] \qquad \text{(B2)}$$

$$h_r + h_1 = s \sin \delta_1$$

$$h_r = s \sin \delta_1 - h_1 \qquad \text{(B3)}$$

s	dip slip displacement, m.
δ_1, δ_2	angle between modern river and fault above and below the fault bend, degrees.
α_1, α_2	angle between modern river and strata, degrees.
h_1, h_2	height of terrace above river, m.
γ	orientation of axial surface computed by $\gamma = (\alpha_1 + \alpha_2)/2$
ψ	angle of the backlimb, degrees.
λ	length of the backlimb of the folded terrace: $\lambda = (h_1-h_2) / \sin \psi$
$r(t), r(t_o)$	profile of modern river and river at time of terrace formation, t_o
h_r	change in height of river since initial terrace formation t_o, m.

Figure B1. (a) Schematic illustration of terrace deformation predicted by fault-bend fold theory [*Suppe*, 1983]. The strath terrace is an unconformity that is displaced along with underlying layered strata that deform by slip on a fault. The diagram illustrates the case for strata oriented parallel to the underlying fault (α=δ), an assumption we make in this study for the Issyk-Ata and Akchop Hills faults (Alamedin and Djuanarik river terraces, respectively). A constant magnitude of slip, *s*, occurs along the fault surface; bedding-parallel shear within the Neogene strata accommodates slip across the fault bend. The profile of the river terrace at its time of formation, $r(t_o)$, is indicated by the dashed line, here shown to indicate a relative rise in river level since the time of terrace formation. (b) Equation B1 shows the calculation of displacement from the change in terrace height across the fault bend and the dips of the underlying fault. Also derived is the relationship between the angle of the backlimb of the terrace, ψ, and the fault dips δ_1 and δ_2 (Equation B2). The amount of relative vertical change of the river, h_r, since the terrace was formed, is derived in Equation B3.

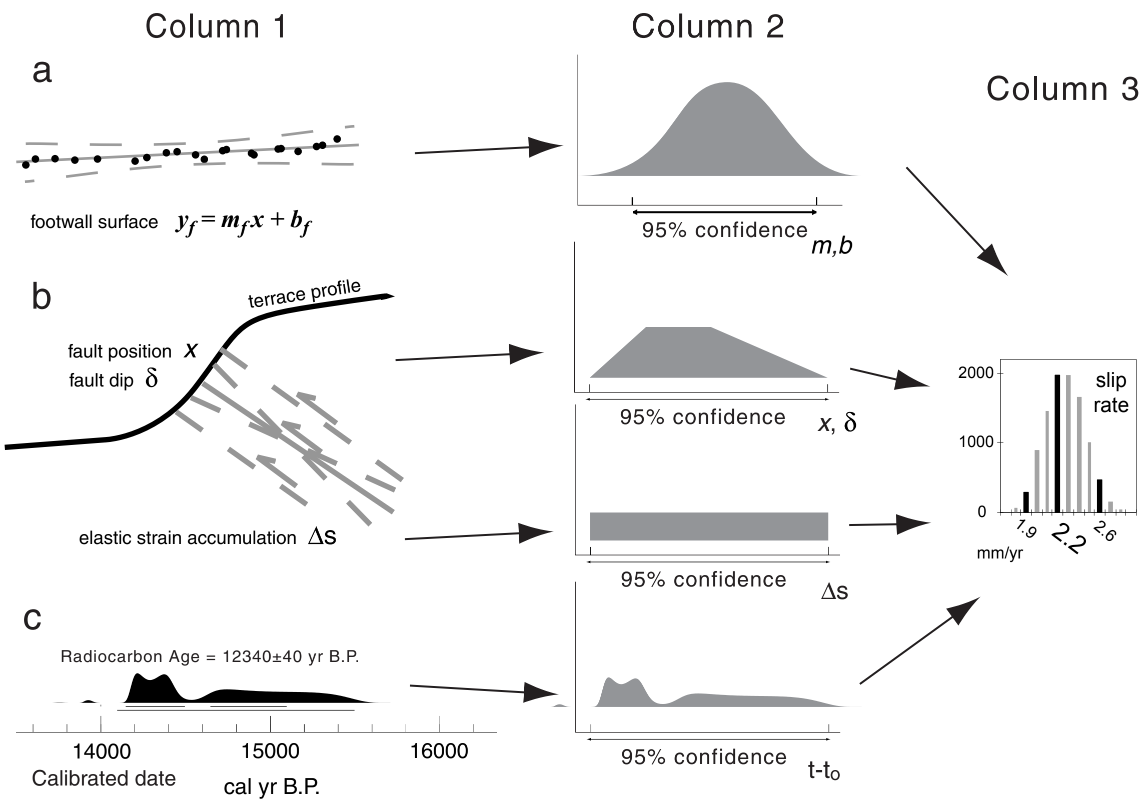

Figure C1. Calculation of uncertainties from measurements of slip rate variables. Column 1 indicates measurements made in the field or laboratory, and Column 2 shows the probability representations of the different variables that go into the Monte Carlo simulation. (a) Linear regression of survey points on a terrace represents a hanging wall or footwall. Solid line indicates least-squares fit and dashed curved lines represent 95% confidence ranges given standard errors in slope, *m*, and intercept, *b*. (b) Measurements or constrains on the dip, δ, and location of a fault projecting onto a scarp, *x*, are represented by normal, uniform, or discrete distributions. A trapezoidal distribution is shown here. Elastic strain accumulation, Δs, is represented by a uniform distribution. (c) Calibration of a radiocarbon age, showing probability density of calibrated ages. The discrete probability density of the calibrated age is represented in the error analysis if the offset unit is constrained by one radiocarbon age. Column 3 shows an example of a histogram of slip rate. The slip-rate numbers that correspond to black histogram bars are midpoints for bins, and indicate the most probable value and 95% confidence limits.

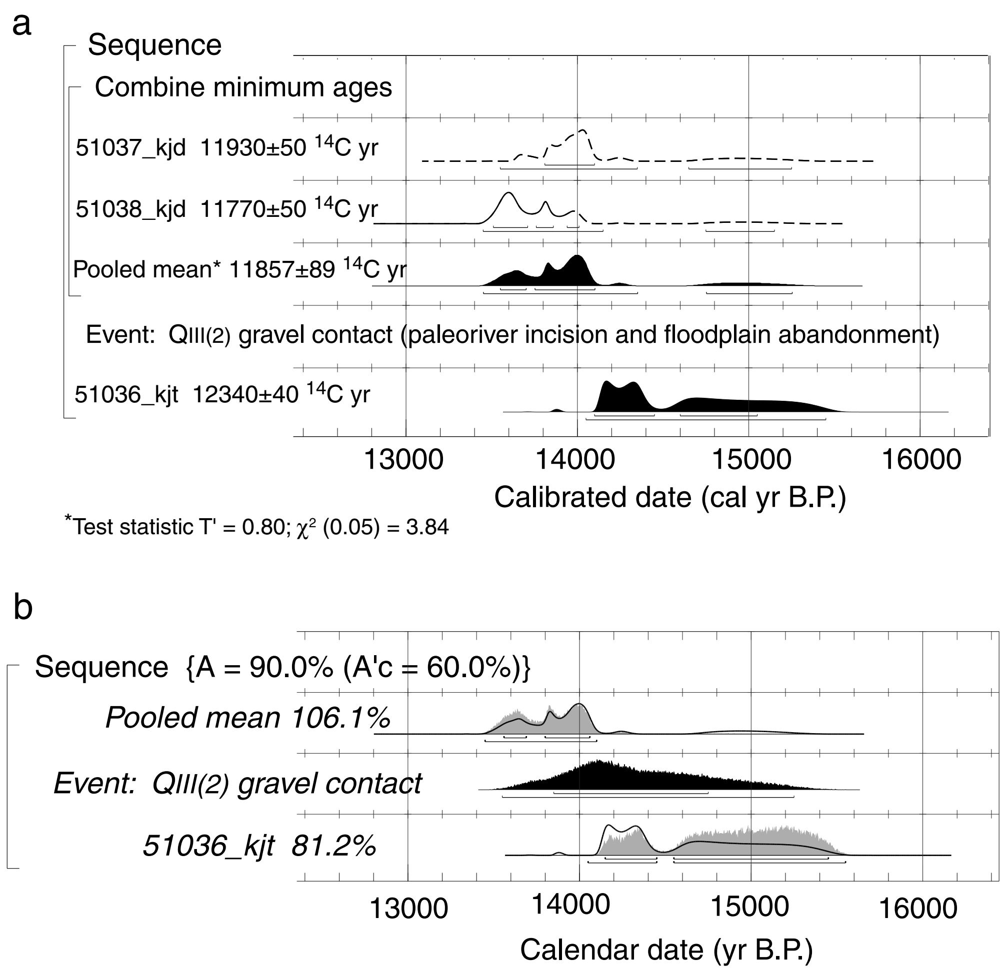

Figure C2. Age analysis of the QIII(2) terrace at the Kadjerty River, Naryn basin, using the publicly available program OxCal 3.5 [*Ramsey*, 1995]. The goal is to statistically describe the age distribution of the terrace forming "event," which is represented by the contact between coarse gravel and overlying silt and sand. (a) Radiocarbon sample ages and calibrated age distributions for three detrital charcoal samples. Overlying the "event" is the calibrated age distribution of the pooled mean radiocarbon age of two statistically similar detrital charcoal samples collected from above the gravel contact (similarity test described in *Ward and Wilson* [1979]). Calibrated ages of the individual charcoal samples are shown above by dashed lines. Underlying the "event" is the calibrated age of the charcoal sample collected below the gravel contact. (b) Age analysis of the "event" using Bayesian statistical methods described by *Ramsey* [1998]. The calibrated age distributions of the original samples above and below the event are in black lines. Grey area indicates the reweighted age distribution based on the additional constraint of stratigraphic order. The *a posteriori* age distribution of the "event" is determined from the reweighted distributions of the sample ages and an unconstrained *a priori* distribution of the "event". The agreement index indicates the extent to which the final (*a posteriori*) sample age distribution overlaps with the original (*a priori*) sample distribution. Index values below 60% are questionable (this level of disagreement is very similar to that for the 5% level chi squared test). In this example, the overall agreement index A exceeds the critical agreement A'c.

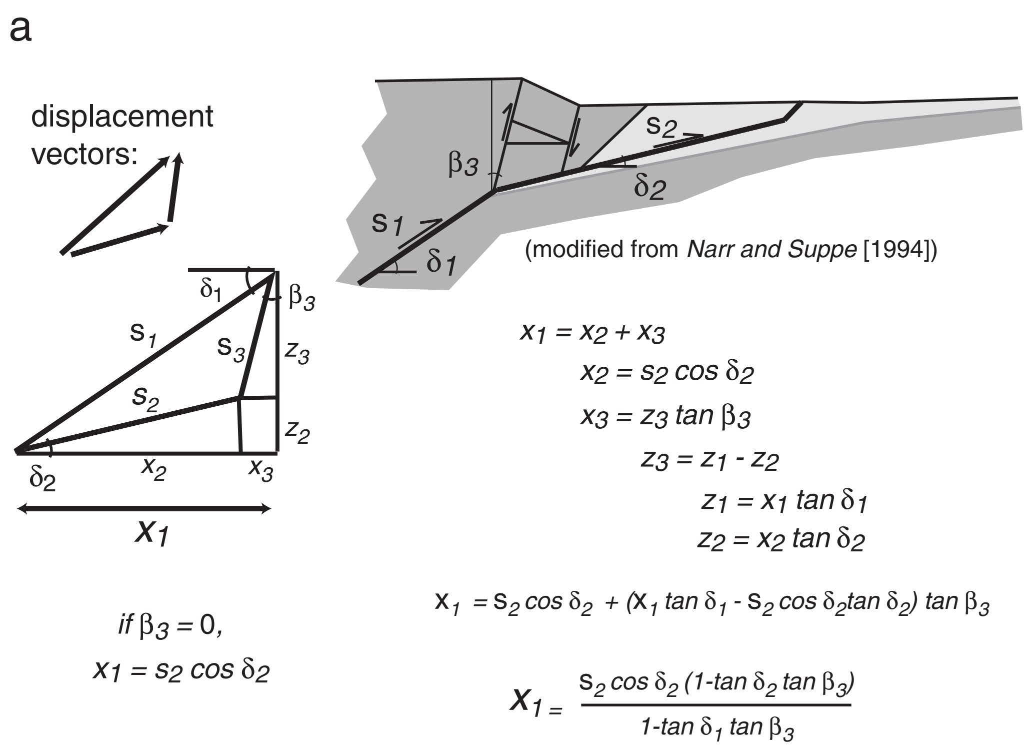

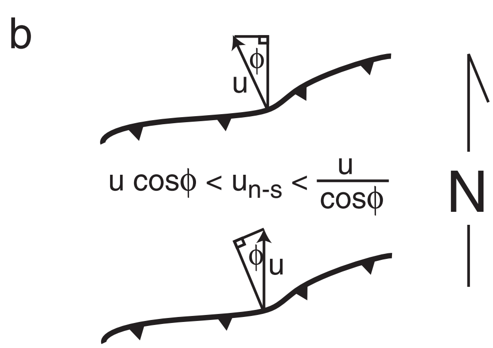

Figure D1. Conversion from fault dip slip to horizontal shortening. (a) Relationship between amount of horizontal shortening x_1 and slip s_2 on a shallow fault that dips at an angle δ_2. (b) North component of shortening rate $u_{n\text{-}s}$ constrained to between the pure dip slip direction and due north-south.

Table 1. Radiocarbon ages and calibration of charcoal samples

Sample code Lab number[1,2]	Radiocarbon age[2,3,4] ^{14}C yr (±1σ)	Calibrated age ranges[5] cal yr B.P. (95%)	Area[6]	Location; Stratigraphic unit; (site name)	Height above gravel contact; (height above lower contact of unit), m
SCT/090899/8(4) 59758	11880 ± 40	13620-14100 14230-14260 14780-14830	0.978 0.011 0.011	Alamedin R., Chu basin; QIII(3) terrace	+0.50
SCT/090899/8(5) 59760	11860 ± 50	13550-14100 14230-14260	0.993 0.007		+0.50
99/Koch/2e 57622	11700 ± 50	13450-13900 13940-13960	0.996 0.004	Djuanarik R., Kochkor basin; QIII(2) terrace	+1.10
99/Kurtka/5 57606	12160 ± 50	13830-13950 14050-14370 14620-15340	0.094 0.521 0.385	Kadjerty R., Naryn basin; QIII(3) terrace	+0.10
99/Kurtka/10 57607	12190 ± 80	13830-13950 14040-14390 14600-15380	0.077 0.502 0.421		+0.15
98/Kadj/1 51037	11930 ± 50	13640-14110 14220-14260	0.982 0.018	Kadjerty R., Naryn basin; QIII(2) terrace; (Terrace tread gully exposure)	+0.30
98/Kadj/2 51038	11770 ± 50	13490-14020	1.000		+0.10
98/KadjQ3tr/11 51036	12340 ± 40	14110-14440 14540-15430	0.433 0.567	Kadjerty R., Naryn basin; QIII(2) terrace; (Fault scarp gully)	-0.10
98/Odjar/100 51044	8180 ± 50	9010-9290	1.000	Oinak-Djar fault trench, At-Bashi basin; Layer A	(+0.05)
98/Odjar/8 51039	8790 ± 40	9600-9940 9990-10150	0.913 0.087	Oinak-Djar fault trench, At-Bashi basin; Layer C	(+0.25)
99/Odjar/104 51040	9140 ± 50	10210-10420 10460-10470	0.983 0.017		(+0.20)

Notes:

[1]Samples prepared and run at Center for Accelerator Mass Spectrometry, Lawrence Livermore National Labs.

[2]Delta ^{13}C values of -25 are assumed according to *Stuiver and Polach* [1977].

[3]The quoted age is in radiocarbon years using the Libby half-life of 5568 years and following the conventions of *Stuiver and Polach* [1977].

[4]Sample preparation backgrounds have been subtracted, based on measurements of samples of ^{14}C-free coal. Backgrounds were scaled relative to sample size.

[5]Calibration with CALIB [*Stuiver and Reimer*, 1986] version 4.3 using corrections in *Stuiver et al.* [1998].

[6]Relative area under the probability distribution that lies within the 95% confidence limits.

Table 2. TL and IRSL data and ages of QII(2) terraces

Sample code Lab number [a,b]	Dose rate [c], D_R ±1σ (Gy/ka)	Mode	Preheat [d]	Bleach [e]	Equivalent dose [g], D_E ±1σ (Gy)	Time/Temp [h] (s)/(°C)	Age [i] ±1σ (ka)	Location	Material; thickness of deposit (m) Height above gravel (m)
SCT/090899 TIEN99-1	5.55±0.60	IRSL	160°C/2d	780/2h	943±96	1-10s	170±25	Alamedin R., Chu basin	Silt; 30 2.65
98-Koch-Q2 TIEN98-1	5.01±0.32	IRSL IRSL TL TL	150°C/2d 170°C/2d 160°C/2d 160°C/2d	780/2h 780/2h 400/3d FSL/8h	679±76 [f] 589±81 [f] 644±79 [f] 742±91	1-10s 1-50s 330-210°C 330-210°C		Djuanarik R., Kochkor basin	Silt; 4 0.20
		Weighted mean of *f* = 639±45					128±13		
SCT/091699 TIEN99-2	4.45±0.34	IRSL	160°C/2d	780/2h	667±87	1-40s	150±23	Djergetal R., Naryn basin	Sandy silt; 2.7 0.30
SCT/091899 TIEN99-3	4.51±0.26	IRSL TL	160°C/2d 145°C/2d	780/2h FSL/6.5h	423±35 644±57	1-30s 260-390°C	93.8±9.0 [k] 143±15	Djergetal R., Naryn basin	Sandy silt; 1.7 0.30

Notes:

[a]Sample preparation and measurements at the Desert Research Institute, Reno.

[b]Polymineralic, non-carbonate, detrital 4-11 μm diameter size fraction was used for all TL and IRSL measurements. Luminescence was detected at the 420±20 nm spectral region (bandpass 390-470 nm at 1% cut). Laboratory sample-preparation procedures follow *Berger* [1990].

[c]Effective dose rate, D_R, is derived from independent measurements of U, Th, K and water concentration. D_R is calculated with the conversion factors and equations given by *Berger* [1988], and includes a cosmic ray component varying from 0.03 to 0.17 with estimated average depth, from the data of *Prescott and Hutton* [1988].

[d]The chosen pre-readout heating and duration (days) (to empty laboratory-filled electron traps). Pre-heating was applied after bleaching.

[e]Bleaching protocol (FSL = full solar spectrum at Reno; 400 = laboratory Hg-vapor lamp with 400-750 nm passed; 780 = > 780 nm solar spectrum passed), and duration (hours or days)

[g]Weighted mean equivalent dose plus average error over time/temperature interval in the next column. A weighted-saturating-exponential regression and error model [*Berger et al.,* 1987] was employed for all samples. For some IRSL samples, inter-aliquot scatter was minimized by short-shine normalization (to natural signals) [*Ollerhead et al.,* 1994].

[h]The readout (LED-on) time interval or the temperature interval (if TL) for which D_E is calculated

[i]Luminescence age $t = D_E / D_R$

[k]Measurement rejected because it is significantly different from the TL measurement of the same sample, and the TL age is not significantly different from the age of sample TIEN99-2, collected from a stratigraphically similar terrace ~1.5 km away [*Thompson et al.*, manuscript in preparation].